Quaternary Science Reviews 215 (2019) 213–231

Contents lists available at ScienceDirect

Quaternary Science Reviews

journal homepage: www.elsevier.com/locate/quascirev

Chronostratigraphic model of a high-resolution drill core record of the past million years from the Koora Basin, south Kenya Rift: Overcoming the difficulties of variable sedimentation rate and hiatuses

A.L. Deino [a, *], R. Dommain [b, c], C.B. Keller [a, d], R. Potts [b], A.K. Behrensmeyer [e], E.J. Beverly [f], J. King [g], C.W. Heil [g], M. Stockhecke [h], E.T. Brown [h], J. Moerman [b], P. deMenocal [i, j], the Olorgesailie Drilling Project Scientific Team[1]

[a] Berkeley Geochronology Center, 2455 Ridge Road, Berkeley, CA 94709, USA
[b] Human Origins Program, National Museum of Natural History, Smithsonian Institution, Washington, DC 20013-7012, USA
[c] Institute of Geosciences, University of Potsdam, Karl-Liebknecht-Straße 24-25, 14476 Potsdam-Golm, Germany
[d] Department of Earth Sciences, Dartmouth College, Hanover, NH 03755, USA
[e] Department of Paleobiology, National Museum of Natural History, Smithsonian Institution, Washington, DC 20013-7012, USA
[f] University of Houston, Department of Earth and Atmospheric Sciences, Science & Research Building 1, 3507 Cullen Blvd, Rm. 312, Houston, TX 77204-5007, USA
[g] Graduate School of Oceanography, University of Rhode Island, South Ferry Road, Narragansett, RI 02882, USA
[h] Large Lakes Observatory, University of Minnesota Duluth, Duluth, MN 55812, USA
[i] Department of Earth and Environmental Sciences, Columbia University, Palisades, NY 10964, USA
[j] Lamont-Doherty Earth Observatory, Columbia University, Palisades, NY 10964, USA

ARTICLE INFO

Article history:
Received 27 February 2019
Received in revised form
6 May 2019
Accepted 10 May 2019
Available online 29 May 2019

Keywords:
Pleistocene
Paleolimnology
East Africa
Sedimentology
Radiogenic isotopes
Bayesian modeling
paleosol
Tephrostratigraphy
Magnetostratigraphy
Kenya Rift

ABSTRACT

The Olorgesailie Drilling Project and the related Hominin Sites and Paleolakes Drilling Project in East Africa were initiated to test hypotheses and models linking environmental change to hominin evolution by drilling lake basin sediments adjacent to important archeological and paleoanthropological sites. Drill core OLO12-1A recovered 139 m of sedimentary and volcaniclastic strata from the Koora paleolake basin, southern Kenya Rift, providing the opportunity to compare paleoenvironmental influences over the past million years with the parallel record exposed at the nearby Olorgesailie archeological site. To refine our ability to link core-to-outcrop paleoenvironmental records, we institute here a methodological framework for deriving a robust age model for the complex lithostratigraphy of OLO12-1A. Firstly, chronostratigraphic control points for the core were established based on $^{40}Ar/^{39}Ar$ ages from intercalated tephra deposits and a basal trachyte flow, as well as the stratigraphic position of the Brunhes-Matuyama geomagnetic reversal. This dataset was combined with the position and duration of paleosols, and analyzed using a new Bayesian algorithm for high-resolution age-depth modeling of hiatus-bearing stratigraphic sections. This model addresses three important aspects relevant to highly dynamic, non-linear depositional environments: 1) correcting for variable rates of deposition, 2) accommodating hiatuses, and 3) quantifying realistic age uncertainty with centimetric resolution. Our method is applicable to typical depositional systems in extensional rifts as well as to drill cores from other dynamic terrestrial or aquatic environments. We use the core age model and lithostratigraphy to examine the interconnectivity of the Koora Basin to adjacent areas and sources of volcanism.

1. Introduction

A suite of hypotheses has been generated that propose direct links between past environmental change and hominin evolution in Africa (Vrba, 1992; deMenocal, 1995; Potts, 1996, 2013). Rigorously testing any such models requires long and robust

* Corresponding author.
E-mail address: adeino@bgc.org (A.L. Deino).

[1] Olorgesailie Drilling Project Scientific Team (additional members): D. Deocampo, Y. Garcin, N.E. Levin, R. Lupien, R.B. Owen, N. Rabideaux, J.M. Russell, J. Scott, S. Riedl, K. Brady, J. Bright, J.B. Clark, A. Cohen, J.T. Faith, A. Noren, V. Muiruri, R. Renaut, S. Rucina, K. Uno.

https://doi.org/10.1016/j.quascirev.2019.05.009
0277-3791/

environmental and climatic reconstructions that are precisely dated. Reliable absolute chronologies are particularly relevant when environmental reconstructions are to be temporally correlated with the archeological and fossil record. Until recently, sufficiently long paleoenvironmental records that could be related to hominin evolutionary changes were mainly derived from marine sediment cores (e.g., deMenocal, 1995). While marine cores provide stratigraphically complete and long records, they can be susceptible to low sedimentation (i.e., low temporal resolution) and may integrate climatic and environmental signals over large spatial domains, thus limiting clear linkages between derived climatic/environmental signals and paleoanthropological observations. By contrast, outcrop paleoenvironmental records directly retrieved from African fossil sites are typically stratigraphically incomplete, short in duration, and prone to variable degrees of time-averaging of environmental indicators such as fossil remains (Behrensmeyer and Hook, 1992).

In an effort to fundamentally improve the understanding of East African environmental change across critical intervals of hominin evolution, a number of drill cores were recently collected from subaerially exposed rift basins along the eastern arm of East African Rift System (EARS), mostly in close proximity to important fossil sites as part of the Hominid Sites and Paleolakes Drilling Project (HSPDP) (Gibbons, 2013; Pennisi, 2013; Cohen et al., 2016; Campisano et al., 2017). These cores contain environmental records on the order of $>10^5$–10^6 years duration (e.g., Sier et al., 2017). However, in contrast to marine or continuous lacustrine sedimentary environments, subaerially exposed basins are directly affected by various Earth surface processes such as flooding, episodic deposition and sediment reworking, weathering, soil formation, deflation, and fluvial erosion that collectively can produce highly variable sedimentary packages and challenge the development of precise chronologies.

In addition, an array of rift-specific processes further complicate simple age-depth relationships of sedimentary deposits in the tectonically and magmatically active EARS. On larger time-scales, extensional tectonism continuously creates accommodation space in the rift as a whole (e.g., Hendrie et al., 1994; Ebinger et al., 2012; Melnick et al., 2012). However, individual events of seismicity and associated normal faulting usually are focused within a localized axis of volcano-tectonic activity (e.g.,Strecker et al., 1990; Gawthorpe and Leeder, 2000). As this axis migrates towards the rift center over time, the rift becomes internally compartmentalized into sub-basins that experience more individualized and episodic tectonism and sedimentation (Baker, 1986). This rift segmentation can modify catchments by rerouting rivers (Bergner et al., 2009) and may suddenly increase sediment flux or alternatively may isolate basins and force sediment starvation (Behrensmeyer et al., 2018).

Moreover, EARS-associated volcanism, in particular the formation of inner-rift volcanic centers during the Pleistocene, led to the episodic release and deposition of pyroclastic deposits. These may be voluminous, and either directly deposited as fallout, surge, or ignimbrites, or fluvially retransported to basins, producing pulses of high sedimentation (e.g.,Trauth et al., 2003; Blegen et al., 2016; Deino et al., 2018). Regionally, the Koora Basin is within the depositional 'sphere of influence' of three major centers active over the past ~1 Ma (Fig. 1): 1) the Ol Doinyo Nyokie dome ignimbrite complex (Baker, 1975) just SE of the drill site, 2) the nepheline carbonatite volcanoes of Embagai, Kerimasi, and Ol Doinyo Lengai in the northwestern Ngorongoro Volcanic Highlands (Foster et al., 1997; Mollel and Swisher, 2012; Sherrod et al., 2013; Mana et al., 2015), and 3) a group of five volcanoes or vent areas in the Central Kenya Rift near Lake Naivasha (Suswa, Longonot, Olkaria, Eburru, and Menengai; Macdonald and Scaillet, 2006). The influence of volcanism in the Koora basin may have shifted over time due to the waxing and waning of explosive activity at these centers, as well as due to shifting basin connectivity and drainage areas as volcanic edifices were constructed or eroded, or tectonism deformed the landscape.

Interacting with these volcano-tectonic controls on sedimentation in the rift are orbitally driven hydroclimatic cycles (e.g.,Deino et al., 2006; Verschuren et al., 2009). Rift sub-basins are often highly sensitive to hydroclimatic change (Olaka et al., 2010). During dry-wet transitions, rift basins experience pronounced shifts from subaerial or shallow lacustrine to deep lacustrine conditions, with substantial changes in sediment production (Garcin et al., 2009). Transitions from dry to wet climatic intervals are apparently also characterized by short-lived non-linear pulses of erosion, sediment transport and deposition (Garcin et al., 2017).

These climate and rift-related processes result in complex sedimentary sequences in which deposition times for different units may be highly uneven (Trauth, 2014). Simple linear or polynomial age-interpolation of longer dated sequences from active rift settings is unlikely to yield accurate age estimates and can potentially result in skewed time-series. A major challenge with drill cores from the EARS is thus to disentangle the complex suite of sedimentary units and their varying deposition times in pursuance of generating robust time-series of environmental dynamics that can be accurately correlated with outcrop-based paleoecological and archeological records. Currently available drill-core records from the EARS contain inadequate dating densities to fully overcome this challenge and do not sufficiently consider the uncertainties of their age models (e.g.,Scholz et al., 2007; Foerster et al., 2012; Johnson et al., 2016; Lupien et al., 2018). Here we present a densely dated drill core, rich in lithological units from the Koora Basin in the south Kenya Rift, collected as part of the Olorgesailie Drilling Project. This is the first core from the EARS to address strongly varying deposition times and associated age-model uncertainties.

The Olorgesailie Basin, north of the Koora Basin and connected via the Koora Graben (Fig. 1), contains outcrops dated ~1.2 to 0.04 Ma that preserve a long sequence of archeological and fossil sites (Deino and Potts, 1990; Potts, 1994; Behrensmeyer et al., 2002). These sites provide evidence of marked changes in hominin behavior, mammalian fauna, and depositional regimes during the period from ~500 ka to 320 ka (Behrensmeyer et al., 2018; Brooks et al., 2018; Deino et al., 2018; Potts et al., 2018). This time interval of ~180-kyr is, however, represented by an erosional hiatus in the outcrop record, thus sedimentary and paleoenvironmental data are unavailable that could otherwise provide context for the evolutionary transitions. The adjacent Koora Basin was investigated by the Olorgesailie Drilling Project as a potential accumulation area of deposits that temporally overlap those of the Olorgesailie Basin. Ground magnetic prospecting conducted in 2009 and seismic reflectance tests in 2011 suggested that sedimentary deposits of >100 m depth to basement rock were present in the Koora Basin.

Two sediment cores encompassing the time of the erosional hiatus at Olorgesailie were recovered from the Koora Basin as part of the Olorgesailie Drilling Project. The first of these cores, 24 km south of the Olorgesailie outcrops, was drilled to a depth of 166 m at borehole site OLO12-1A. The purpose of this paper is to document the development of a detailed chronostratigraphic age model for this core that will be used to provide absolute age calibration of core records. We discuss our methodology for building the age model: 1) establishing a set of chronostratigraphic age/depth points based on $^{40}Ar/^{39}Ar$ dating and paleomagnetic reversal stratigraphy; 2) establishing a hiatus record by identifying and characterizing paleosols (fossil soils); 3) compensating for 'event deposits' and rapid sedimentation when assessing stratigraphic

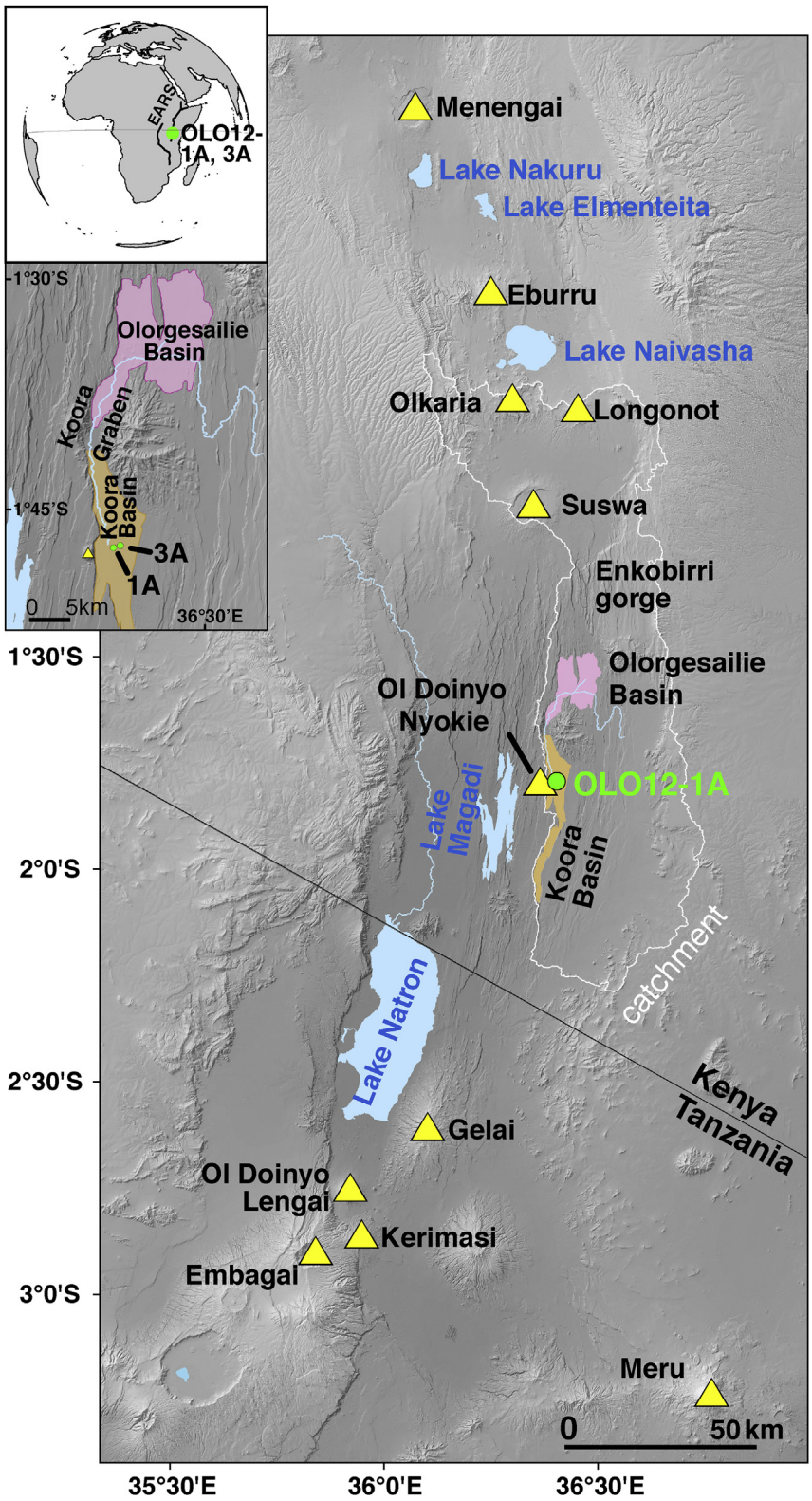

Fig. 1. Map of south-central Kenya and northern Tanzania, showing the location of the OLO12-1A and OLO12-3A cores (green circles), about 24 km south of the Olorgesailie archeological site. The Olorgesailie Basin is highlighted in pink, and the Koora Basin in brown. Volcanoes active within the last ~1 Ma are identified by yellow triangles. The present catchment of the Koora Basin is outlined in white, extending north and eastward, but separate from the adjacent Lake Magadi basin to the west. Elevation data are based on the TanDEM-X Science DEM (© DLR 2017). (For interpretation of the references to color in this figure legend, the reader is referred to the Web version of this article.)

accumulation rates based on smear-slide assessment of volcanic glass abundance; and 4) inputting these data into a Bayesian stratigraphic age model calculated at high resolution that specifically incorporates hiatuses. Finally, we use the results of the model to interpret the southern Kenya Rift basin history, including volcanic sources and basin connectivity, in the past ~1 Ma.

2. Methods

We address the challenges in deriving precise chronologies from complex lithostratigraphic sequences by establishing a methodological framework to obtain a robust chronostratigraphic model for the sedimentary record of OLO12-1A (Pennisi, 2013). Chronostratigraphic control points for the core were established based on K-feldspar $^{40}Ar/^{39}Ar$ ages on intercalated tephra deposits and a lava flow from the base of the core, as well as magnetostratigraphic measurements identifying the precise stratigraphic position of the Brunhes-Matuyama geomagnetic reversal. The resulting dataset is combined with the position and duration of paleosols and modeled using a new Bayesian algorithm for high-resolution age-depth modeling of hiatus-bearing stratigraphic sections, with a prior constraint of adherence to the law of stratigraphic superposition. This model addresses three important aspects relevant to highly dynamic, non-linear depositional environments: 1) correcting the original depth of litho-stratigraphic units for variable rates of deposition, 2) accommodating intervals of non-deposition (hiatuses) represented by paleosol development, and 3) quantifying age uncertainty with centimetric resolution.

2.1. Core collection and lithostratigraphic description

Between September 3 and 15, 2012, two drill cores were retrieved from the Koora Basin (Fig. 1) by Drilling and Prospecting International Ltd. (DPI) with a truck-mounted PRD Multistar drilling rig equipped with Boart Longyear HQ3 and HQTT tooling. Three meter long and 61 mm diameter cores were collected in polycarbonate liners and divided on site into 1.5 m long sections for transport and processing. OLO12-1A (1°47′27.60″S, 36°24′4.07″E) was drilled from 27.00 to 166.14 m below surface (mbs) with a recovered total core length of 130.76 m (94% recovery). Due to the unconsolidated nature of surficial sediments, the upper 27 m of the bore hole 1A were destructively recovered by reverse-circulation drilling and collected as 1 m bulk samples. About 900 m east of OLO12-1A a second core, OLO12-3A (1°47′19.36″S, 36°24′30.60″E), was recovered from 50 to 116.27 mbs with a total length of 66.73 m (recovery 100%) (Fig. 1). This study focuses on the age model of OLO12-1A but uses stratigraphic information from OLO12-3A to help identify rapidly accumulated event deposits.

Cores were shipped to the National Lacustrine Core Facility, University of Minnesota, Minneapolis (LacCore) for processing, description, scanning, subsampling, and permanent cold storage during the 'Initial Core Description' (ICD) workshop in April, 2013. Cores were longitudinally split with a tile saw into working and archive halves, and fresh split cores were photographed with a Geotek MSCL-CIS optical linescan camera at 50 μm resolution. X-ray radiographs were obtained from the surfaces of archive halves with an ITRAX X-ray core scanner at the Large Lakes Observatory (University of Minnesota-Duluth).

During the ICD we used a combination of macroscopic observations and smear-slide analysis (Kelts, 2003) to designate lithostratigraphic units. Each 1.5 m core section along with its accompanying high-resolution image was visually inspected by AKB and RBO for sediment type (e.g., sand, silt, clay), color, sedimentary structures, bedding boundaries, and reaction to 10% HCL. These criteria were used to define successive sedimentary units, and additional observations were made at regular intervals to detect gradational changes within the thicker units. The split-core surface was often affected by saw marks or other alterations such as differential moisture and drying, and we used the high-resolution images in tandem with the core itself for macroscopic descriptions. Smear-slide observations were used for detailed information on grain size, mineralogy, and microfossil content. Visual description also included core-catcher pieces from the core ends.

For smear-slide analysis, we collected tiny amounts of sediment with a toothpick and placed it on a glass slide with deionized water at approximately every 50 cm of core and at pronounced changes in lithology. After drying on a hotplate, Norland optical cement 61 was added, the slide covered with a slip and cured under UV light. We examined 243 smear slides with a Leica petrographic microscope for their organic matter content (e.g., algal remains, plant fragments, pollen, spores, charcoal), siliceous microfossils (e.g., diatoms, phytoliths, sponge spicules) and all minerals, including clay, and bulk clastics such as carbonates and volcanic glass. The percentages of every component of the whole sample were visually estimated for each slide, providing a semi-quantitative measurement of sediment composition. Unknown minerals and other sedimentary matter were identified with support from LacCore scientists and reference materials (CSDCO, 2011; Rothwell, 1989). We counted an additional 101 smear slides from a narrow interval of the upper part of the core solely for evaluation of volcanic glass abundance relative to all other components. Smear-slide information was added to the macroscopic sediment descriptions on the ICD sheets by AKB.

2.2. $^{40}Ar/^{39}Ar$ dating methods

OLO12-1A contains numerous tephra deposits with distinct depositional character and stratigraphic spacing suggesting that they represent discrete eruptive events or merged eruptive sequences. They range in thickness from less than 1 mm to 10.6 m. Although tephra are present sporadically in the early history of the basin, more abundant and coarser tephra are concentrated primarily in the upper half of the core. $^{40}Ar/^{39}Ar$ dating of K-feldspar phenocrysts extracted from these tephra provide almost all of the new radiometric ages reported herein, with the addition of a $^{40}Ar/^{39}Ar$ date on K-feldspar phenocrysts from a trachyte flow at the base of the core, representing the local basement.

Sampling of the core for datable material was carried out at LacCore during the ICD. Tephra horizons were identified by direct visual inspection of the working and archival core halves, immediately following core splitting in order to best observe subtle variations in color and texture, before inevitable oxidation and drying of the cores. Where megascopic identification of pyroclasts was ambiguous, potential tephra horizons were examined for the presence of glass shards and phenocrysts using smear slides, and occasionally with SEM microscopy to examine pyroclastic textures aided by EDS analysis to verify the presence of K-feldspar (Hitachi TM-1000 desktop scanning electron microscope). In total, 91 samples were obtained from the working core halves for further processing at the Berkeley Geochronology Center (BGC). Note that the upper 27 m of the core was augured and not sampled for tephrostratigraphy or dating due to disturbance of the stratigraphy.

Tephra samples were processed at BGC to obtain the coarsest, freshest, and most inclusion-free K-feldspar mineral grains for single-grain $^{40}Ar/^{39}Ar$ analysis. Initial mineral separations of tephra samples consisted of gentle disaggregation and wet sieving using distilled water through a new 90 or 400 μm sieve bag, depending on mineral grain size, retaining all components. K-feldspar in the coarser fraction was concentrated with a Frantz magnetic separator if necessary, hand-picked under a binocular microscope, washed in

5% HF and distilled water, and hand-picked again to obtain the clearest, most inclusion-free material. In some cases the final hand picking was done with the grains submersed in water, which facilitated a clearer view of the interior of grains, hence helping in avoid inclusions. Typically, it was unnecessary to use heavy liquids to separate plagioclase from K-feldspar, as most tephra contained only anorthoclase as the feldspar component. Plagioclase phenocrysts were not included in the dating mineral separates, as the low potassium content for <1 Ma age material leads to low radiogenic ^{40}Ar signals in the mass spectrometry step and unacceptably large single-grain age uncertainties. Feldspar grain sizes ranged from 200 μm to 2 mm. Feldspar from the lava flow at the bottom of the core was separated using similar methodology, consisting of hand-crushing, HF cleanup, and hand-picking. Not all samples obtained at LacCore were dated; some yielded insufficient K-feldspar or were considered redundant due to coverage by other closely spaced samples. In total, 28 separates of K-feldspar from 21 tephra units and one lava flow were prepared for $^{40}Ar/^{39}Ar$ dating. Three of the tephra samples were from bulk ash, while 25 were from pumice.

The completed mineral separates were irradiated in the Cd-lined CLICIT position of the Oregon State University TRIGA reactor in four batches of 0.5 h each. All irradiations employed sanidine phenocrysts from the Alder Creek Rhyolite of California (orbitally referenced age = 1.1848–0.0006 Ma; Niespolo et al., 2017) as the neutron fluence monitor mineral. Standards and unknowns were co-irradiated in a circular configuration in wells in an aluminum disk, with standards at the cardinal positions, and either two or three unknowns situated between standards. The appropriate neutron fluence factor (the '*J*' parameter of $^{40}Ar/^{39}Ar$ dating calculations (McDougall and Harrison, 1999); for the unknown positions was calculated from a planar fit of the standard calibrations, with errors derived by Monte Carlo simulation in the predicted *J* value ranging from 0.1 to 0.2% (1σ; Table S1; (Deino et al., 2010). Reactor-induced isotopic production ratios for these irradiations were: $(^{36}Ar/^{37}Ar)_{Ca} = 3.65 \pm 0.02 \times 10^{-4}$, $(^{38}Ar/^{37}Ar)_{Ca} = 1.96 \pm 0.08 \times 10^{-5}$, $(^{39}Ar/^{37}Ar)_{Ca} = 6.95 \pm 0.09 \times 10^{-4}$, $(^{37}Ar/^{39}Ar)_{K} = 3.24 \pm 0.16 \times 10^{-4}$, $(^{38}Ar/^{39}Ar)_{K} = 1.220 \pm 0.003 \times 10^{-2}$, $(^{40}Ar/^{39}Ar)_{K} = 3.5 \pm 0.9 \times 10^{-4}$. Atmospheric $^{40}Ar/^{36}Ar = 298.56 \pm 0.31$ (Lee et al., 2006) and decay constants follow (Min et al., 2000).

Following a period of at least several weeks of radiological 'cooling' after irradiation, the feldspars were analyzed individually by the $^{40}Ar/^{39}Ar$ technique using single-crystal incremental heating (SCIH) at BGC. All argon measurements were performed on a Nu Instruments *Noblesse* noble-gas mass spectrometer, featuring a high-efficiency ionization source and simultaneous multi-isotope measurement using all ion-counting electron multiplier detection systems. In the SCIH technique, individual phenocrysts are incrementally heated in an ultra-high vacuum argon extraction line using a CO_2 laser, in 3–11 steps (depending on grain size and gas yield) at progressively increasing power to fusion. Incremental heating has several advantages to the more common single-step total-fusion analysis, including the ability to efficiently drive off surficial and trapped atmospheric contamination in the initial steps of the experiment, maintenance of fairly consistent gas yields for improved spectrometer detection reproducibility, and most importantly this facilitates examination of the internal argon systematics of the crystal. Incremental heating release plots, in which measured and derived parameters such as percent radiogenic ^{40}Ar content, Ca/K atomic ratio, and apparent age are plotted as a function of the cumulative % ^{39}Ar released during each successive step (Fig. S1), may reveal subtle inhomogeneity or alteration of the grain. Although incremental heating is a time-consuming process, and may result in measurement of fewer grains than a single-step, total-fusion procedure due to analytical time constraints, step-heating experiments have the advantage of identifying material or portions of material that are aberrant in age or composition (e.g., abrupt shifts in Ca/K atomic ratio or the percent ^{40}Ar radiogenic content relative to atmospheric ^{40}Ar) for various reasons (e.g., surficial argon fractionation, alteration, exsolution, micro-inclusions, etc.). These steps or grains can be avoided by requiring that the experiments pass consistency tests (form apparent-age plateaus), and thus can be considered more geologically reliable. A total of 1579 SCIH steps on 294 phenocrysts from 23 samples were analyzed (Table S1). In order to conserve analytical time, the step-heating process was terminated early (after 1–2 steps) for 40 grains that were clearly too old (typically > 1.2 Ma, to as old as 8 Ma), or were plagioclase (two grains); the analytical data for these grains is provided at the end of Table S1.

Most grains carried to completion yielded apparent-age plateaus (Fig. S1). The 'age plateau' identification algorithm used here, similar to that of (Fleck et al., 1977), delineates the set of contiguous steps encompassing the greatest percent of ^{39}Ar release that exhibit an acceptable MSWD ('mean square of weighted deviates,' with a threshold probability >95% that the observed scatter is caused by analytical error alone and that geological scatter is not demonstrated). A plateau must comprise at least 50% of the total ^{39}Ar release and consist of at least three consecutive steps. 'Inverse isochron' regressions ($^{36}Ar/^{40}Ar$ *vs.* $^{39}Ar/^{40}Ar$) were calculated from the plateau steps, and the age derived from this analysis was accepted as the reference age for the particular individual grain (Table S2).

Weighted means were then calculated for the 21 tephra beds recognized as independent stratigraphic units (Table 1). In several cases this required combining sub-samples of an individual bed: multiple individual lapilli (units 1-38-1/2, 1-50-2/1, and 1-57-1/1), or separate levels of the same tuff (unit 1-82-3/1). Further, it was necessary to identify outliers and omit them from the weighted-mean computation in order to identify the primary (eruptive) age of the tephra or flow. Outliers are fairly common, and represent components such as xenocrystic contamination (i.e., detrital contaminants), the presence of excess ^{40}Ar trapped in primary phenocrysts, or subtle alteration not evident during grain selection. Two sequential steps were taken in the outlier-elimination procedure. First, the oldest, definitively xenocrystic grains were located using a 'gap' finding routine. This algorithm proceeds by iteratively testing the oldest analysis against each younger analysis, eliminating the former if the pair exceed an arbitrary 'gap' score (the age difference for each pair of analyses, divided by their joint error combined in quadrature). A gap score of seven was used, which effectively identifies age outliers obvious to a human observer but has minimal effect on distributions that lack a visually pronounced modal gap. Secondly, we employed a robust outlier deletion approach using a 'normalized median absolute deviation from the median' ('nMAD' = 2). Overall, of the 227 incremental heating plateaus, 57 were omitted as outliers from the stratigraphic unit mean ages (Table S2).

2.3. Magnetostratigraphic methods

A total of 21 discrete cube samples were taken between 152 and 162 mbs for paleomagnetic analyses in an effort to identify the Brunhes/Matuyama geomagnetic boundary (BMB, 0.781–0.3 Ma; Ogg et al., 2012). The samples were analyzed using a 2-G® Enterprises small-access cryogenic magnetometer with an in-line alternating field (AF) demagnetization coil in the Paleomagnetics Laboratory at the Graduate School of Oceanography at the University of Rhode Island. The initial natural remanent magnetization (NRM) was measured and the samples subjected to 21 AF demagnetization and measurement steps starting at 3.5 mT and ending at 100 mT (the field was increased by 5 mT between 5 mT and 100 mT) in order to remove any unstable, viscous remanent magnetizations.

Table 1
Chronostratigraphic data set.

Samples	Mean Drilled Depth (mbs)	Mean Z-prime Depth (mbs)	Laboratory ID	n/n_{total}	Age (ka ± 1σ mse)		Tephra Unit Thickness (m)	Description
Surface	0	0			0.05	0.05		Estimated age of present-day surface at drill site
OLO12-1A-29Q-1 75-936	28.50	28.41	26649	6/10	96.8	2.9	0.72	Rounded pumice gravel, clasts to 2 cm
OLO12-1A-31Y-1 33-43	33.70	33.23	26645	8/8	88.0	2.6	0.39	Sub-rounded pumice to 1 cm in mudstone
OLO12-1A-33Q-1119-135	36.80	36.18	26503, 26651	4/5	89.4	2.8	1.39	Rounded pumice to 2 cm in mudstone
OLO12-1A-37Q-1 60-676	46.90	44.58	26505	3/6	208.3	1.4	0.49	Rounded pumice to 1 cm and medium ash in claystone
OLO12-1A-37Q-2 47-586	48.10	45.09	26653	6/7	194.2	6.1	0.67	Coarse ash/fine pumice
OLO12-1A-38Q-1 0-101	49.40	45.75	26650	5/6	165.8	7.3	0.78	Sub-angular pumice to 2 cm in medium-grained black ash
OLO12-1A-38Q-1 43–45 (P1, P2, P3)1	49.80	46.14	26463, 26485, 26496	15/22	181.2	0.7	0.70	Sub-angular pumice to 2 cm in medium-grained black ash
OLO12-1A-40Q-1 60-65	56.00	50.27	26507	9/9	199.8	2.0	0.04	Pumice to 1 cm and fine ash in claystone
OLO12-1A-41Q-1 92-105 P2	59.00	52.27	26508	6/6	209.8	1.8	10.32	Rounded pumice to 2 cm in coarse reworked ash
OLO12-1A-48Q-1 76-84	77.07	58.11	26647	7/8	224.4	1.1	0.11	Sub-rounded pumice in unconsolidated black ash
OLO12-1A-50Q-2132–139 (P1, P3, P4)	82.60	59.65	26472, 26484, 26494	26/35	224.9	0.7	1.78	Sub-angular pumice to 2 cm in fine ash/mudstone
OLO12-1A-52Q-3 93-1002	88.40	64.53	26500	7/9	228.0	1.2	10.67	Sub-rounded to sub-angular pumice to 2 cm in buff volcanic sandstone
OLO12-1A-54Q-2 45-532	93.50	69.23	26471	9/11	225.2	1.3	0.27	Sub-rounded pumice to 3 cm in brown altered mudstone
OLO12-1A-57Q-1 38–44 (P1, P2) 3	101.50	74.59	26470, 26482	13/16	248.6	4.9	4.50	Black sub-rounded pumice to 2 cm in black unlithified coarse ash
OLO12-1A-58Q-2 23-373	104.60	75.25	26643	10/12	245.7	1.5	0.04	Black sub-rounded pumice to 0.5 cm in black coarse ash
OLO12-1A-59Q-1 0-45	107.28	76.71	26511	1/10	326.1	7.1	0.06	Rounded pumice to 2 cm in buff soft mudstone
OLO12-1A-64Q-2 30-36	121.04	90.19	26469	7/10	335.2	2.0	0.56	Several isolated 0.5–1 cm pumice in paleosol
OLO12-1A-71Q-1 23-27	131.90	100.97	26467	5/6	404.6	1.2	0.03	Rare sub-angular black pumice to 1 cm
OLO12-1A-73Q-1 44-47	136.29	105.38	26499	9/12	492.2	13.1	0.33	Sub-angular pumice to 0.5 cm in brown disrupted mudstone
OLO12-1A-80Q-3129-133	149.60	118.63	26501	2/2	605	25	0.82	Tuffaceous grey-brown sandstone
OLO12-1A-82Q-2133–142, OLO12-1A-82Q-3 7-134	152.63	121.49	2,66,41,26,642	2/7	708	34	0.82	Indurated grey tuff with 25–50% sub-angular black pumice to 1 cm
Brunhes/Matuyama Boundary	153.1	121.94			781.0	3.0		Brunhes/Matuyama paleomagnetic boundary
OLO12-1A-89Q-1107-114	166.10	134.67	26468, 27181	10/10	1083.7	4.0	–	Fresh vesicular trachyte flow

Following measurement, the characteristic remanent magnetization (ChRM) declination and inclination values (Kirschvink, 1980) were calculated using the Demagnetization Analysis In Excel (DAIE) tool (Sagnotti, 2013). In order to calculate the ChRM, we selected between 6 and 11 demagnetization steps between 5 and 80 mT and a least-squares fit was made to the selected data points. The fit was not anchored to the origin of the Zijderveld plot (Zijderveld, 1967) since the ChRMs generally trended towards the origin without forcing, and we felt the unanchored option gave a better representation of the data quality demonstrated by the maximum angular deviation (MAD) calculated within the DAIE tool. The criteria for a "quality" ChRM value was that it be calculated from at least three consecutive demagnetization steps and the MAD values were less than 15° (e.g., Tauxe and Badgley, 1988).

2.4. Paleosol characterization and estimation of hiatuses

Accurate stratigraphic age modeling for the purposes of deriving realistic chronologies of core lithostratigraphic, biologic, and geochemical logs requires explicit incorporation of hiatuses. Ignoring hiatuses leads to inaccurate event ages and sediment accumulation rates and thus affect correlations of paleoenvironmental events in a core with those in outcrop or other core records. Fig. 2A illustrates the effect of a hiatus, represented by a paleosol, on the age interval calculated for an example of a possible climate signal (i.e., a diatomite bed). In the illustrated scenario, with a paleosol relatively high in the OLO12-1A section relative to bracketing chronostratigraphic data (two dated tuffs), incorporating a hiatus at a stratigraphic height equal to the top of the paleosol results in a diatomite interval with boundaries that are older and a duration that is shorter than the age model without hiatuses. The hiatus model also has higher sediment accumulation rates above and below the disconformity (essentially 'to make up for lost time'). Fig. 2B illustrates a more complex scenario with two overlapping paleosols lower down in the OLO12-1A sequence. Ages at the hiatuses are both older and younger than the non-hiatus scenario, but again sediment accumulation rates are higher.

Thirty hiatuses were identified in Core 1A, defined by subaerially exposed surfaces or paleosols. The paleosols encompass 31% of the core by thickness. Two parameters were needed as input to the age model: the position of the top of the paleosol, and the duration of pedogenesis (with estimated uncertainty). The tops of paleosols were identified by an abrupt lithologic change in the overlying stratigraphy and loss of soil ped structure, and the base was identified by the reappearance of recognizable parent material lithology (e.g., laminated lacustrine sediments; Fig. 3A).

Estimating the duration of pedogenesis is complicated by the number of factors affecting soil formation. These can be defined by

$$S = f(cl, o, r, p, t),$$

where S is soil, cl is climate, o is organisms living in the soil, r is relief or topography, p is parent material, and t is time (Jenny, 1941).

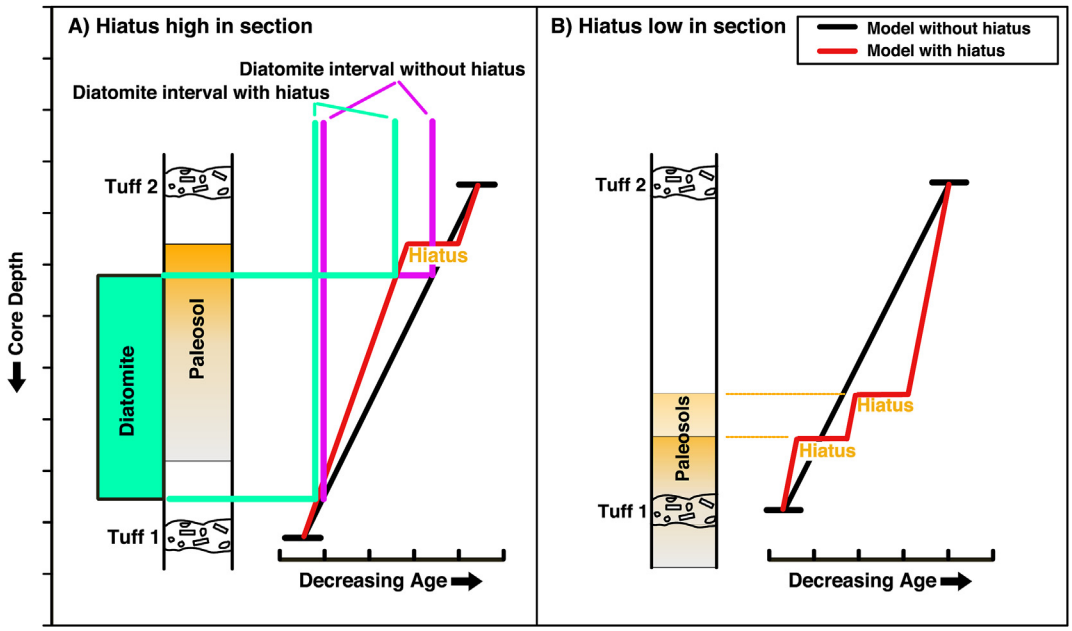

Fig. 2. Schematic representation of the effects of hiatuses between two chronostratigraphic control points on the stratigraphic age model. A) Incorporating the lost time represented by a hiatus (at the top of a paleosol) situated high in a section leads to faster calculated sedimentation rates throughout the section. This results in older model ages for the upper and lower boundary of the example diatomite bed, and a shorter calculated duration of deposition. B) A more complex scenario with two overlapping paleosols relatively low in a section. Ages at the hiatuses are both older and younger than the non-hiatus scenario, but again sediment accumulation rates are higher.

To estimate *t*, certain soil features can be broadly used to approximate the duration of pedogenesis (Targulian and Krasilnikov, 2007). For this project, the estimate of duration is related to a paleosol maturity index (adapted from Cleveland et al., 2007). Each paleosol is classified from 0 to 4 based on the diagnostic soil horizons identified and presence or absence of specific soil features that can be related to duration of soil formation (Table S3 and Fig. 3B).

Critical soil features used to classify these paleosols were: horizonation; the percent of soil carbonate nodules (0, <5%, or >5%); and the presence or absence of vertic soil features (i.e., pedogenic slickensides and wedge peds formed through repeated wetting and drying cycles in soils rich in smectitic clays). The features identified were then used to estimate duration by an order of magnitude, as *cl*, *o*, *r*, and *p* can also affect soil features in addition to *t*. Soil processes identified in the core such as bioturbation can form in 10^0–10^1 years. Weak soil ped formation and horizonation (formation of layers in a soil defined by changes in physical features such as texture or color) can form in 10^1–10^2 years. Strong horizonation, migration of carbonate to form nodules, and vertic soil features form in 10^3–10^4 years (Targulian and Krasilnikov, 2007).

The soil features critical to classification using the paleosol maturity index were described, with each paleosol's index from 0 to 4 corresponding to the estimated duration (Table S4). This duration and the top of each paleosol were then used to indicate locations and durations of each hiatus in the age model.

2.5. Accommodation for variable depositional rates (z-prime depth scale)

The OLO12-1A core is highly variable in terms of sediment composition and structures, with well-bedded lacustrine and fluvial strata alternating with paleosol unconformities, but there also are particular intervals with relatively continuous tephra deposits. Based on detailed core description of the sedimentary structures, lithology, and vertical continuity of these units, we interpret them as representing markedly increased sedimentation rates. We removed or compressed such units within these intervals to derive a corrected depth scale ('z-prime depth') for the purpose of improving our estimates of the chronology of longer-term basin sedimentation (Grimm, 2011; Noren et al., 2002; Stockhecke et al., 2014).

The first step in the process to derive the z-prime depth scale was to remove all intervals containing injection of drilling fluid resulting from breakage of core sections during slow drilling. Second, localized event deposits (e.g., mud flows present in OLO12-1A and not OLO12-3A) were likewise removed (= 100% compression), as is common practice in paleolimnology (e.g., Grimm, 2011; Noren et al., 2002). Third, drilled depths were variably compressed in zones within the core that had a high proportion of tephra mixed with primary lacustrine sediments. Sediment compression or removal was only performed on lithological units thicker than 10 cm, and physical core gaps (no sediment recovery) were not compressed.

Smear-slide analysis revealed that portions of OLO12-1A, in particular the interval between ~50 and 110 mbs, consist largely of tephra – ash, phenocrysts, and minor volcanic lithics. The presence of aquatic indicators (e.g., diatoms) at low proportions in these sequences plus the fine-scale primary lamination, lack of bioturbation, and evidence of sub-aqueous slumping indicates that much of the tephra-rich sediment was deposited over days to years in a lacustrine environment. Instead of compressing or removing every unit that contained large amounts of volcanic glass, therefore, we used a combination of bedding features, grain size and sediment composition to provide a realistic basis for percentage compression.

High-resolution core images and corresponding X-ray radiographs were examined for bedding structure and sediment disturbance. Intervals of weak horizontal bedding or disturbance were further examined for their sediment composition, in particular the abundance of glass shards in smear slides. The following compression rules were applied to such units based on the amount

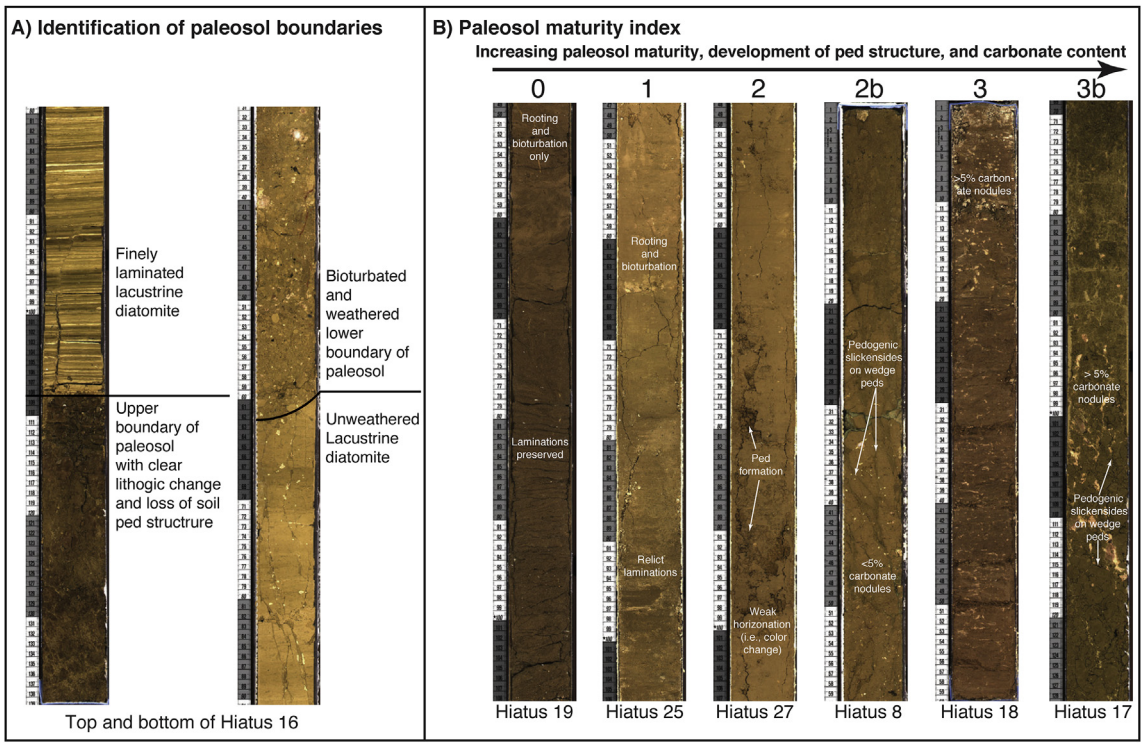

Fig. 3. Paleosol characterization, using examples from OLO12-1A. A) Lithologic criteria for identification of paleosol boundaries: the tops were identified by an abrupt change in the overlying stratigraphy and loss of soil ped structure, while the base was identified by the reappearance of recognizable parent material lithology (e.g., laminated lacustrine sediments). B) Examples of features, such as horizonation, the percent of soil carbonate nodules, and the presence or absence of vertic soil features, used to tabulate the Paleosol Maturity Index (Table S3). Hiatus numbers refer to the paleosol list in Table S4.

of volcanic glass observed: >60%–75% glass = 70% compression; 75–90% = 90% compression; and >90% = 100% compression (i.e., removed). Most compressed intervals were characterized by sand grain size and frequent pumice clasts. We assume that an amount <60% tephra components indicates influx and mixing with other sources, thus slower deposition overall. These intervals were not compressed unless there were other signs of event deposition. Our method for compression represents a new approach for accommodating obvious instances of high sediment influx into a drill-core record, and we expect it to be subject to future testing and modification.

2.6. Volcanic event stratigraphy

As discussed above, the z-prime depth compression methodology utilized identification of very pyroclastic-rich segments of core (>60% tephra). For the purposes of understanding the fuller volcanic record of OLO12-1A, we separately assessed all significant tephra depositional events; i.e., those that appear to be deposited from a continuous accumulation of tephra without significant hiatus. Pyroclastic events were identified by examination of core lithostratigraphy documented during the ICD, semi-quantitative estimation of volcanic shard abundance in smear slides, sampling observations during acquisition of tephra samples for geochemistry and $^{40}Ar/^{39}Ar$ geochronology, visual examination of cores immediately after splitting at the ICD, and follow-up examination of archival photographic scan images of cores. Most pyroclastic deposits in OLO12-1A are reworked ash or pumice deposits likely brought into the basin by fluvial transport of material originally deposited onto the watershed by direct volcanic emplacement (as fallout, surge or ignimbrite). There are also several thin (<2 cm) pure ash beds within lacustrine sequences in the core that are probably direct fallout from ash clouds. Often pyroclastic deposits have discrete tops and bottoms that can be identified by visual examination, but tephra are also commonly mixed with non-volcanic materials, where the tops and bottoms must be estimated based on glass shard abundance. Proceeding upcore, a new pyroclastic event is identified when the ash content reaches 10% or greater; after the peak in ash content is reached, the event is considered terminated when the ash content falls below 15% (rather than 10%, to minimize the effects of delayed deposition of ash). In the longest pyroclastic sequence, multiple pumice lapilli tuffs alternating with vitric tuffs follow unabated for a thickness of ~10.7 m; this was classified as a single volcanic event, though in detail the sequence is composed of multiple eruptive pulses or fluvial pulses closely spaced in time. Likewise, the second longest 'event' deposit (~10.3 m) is likely composed of several closely spaced fluvially redeposited eruptive events that could not be separately distinguished.

2.7. Bayesian age modeling methodology

To construct an accurate, high-resolution chronostratigraphic model of OLO12-1A, we have implemented a Metropolis sampling algorithm for age-depth modeling of stratigraphic sections that explicitly incorporates hiatuses (Keller, 2018). This likelihood-based Markov Chain Monte Carlo model incorporates constraints from (1) the chronostratigraphic age determinations (here, $^{40}Ar/^{39}Ar$ ages on dated volcanic units and a paleomagnetic chron boundary) and (2) estimated hiatus position and duration. Beyond these quantitative constraints, the central assumption of this age-depth model is strict stratigraphic superposition, that is, *lower strata are older*, a constraint which is imposed at the level of each model horizon.

To couple with other datasets derived from the Olorgesailie

Drilling Project cores that are acquired with centimetric resolution, we have designed the final age-depth model to calculate a posterior age distribution for each centimeter of core depth. Consequently, the present inversion includes 13501 model stratigraphic horizons, of which 13467 represent the depth range of interest and the remainder provide a buffer with constant nonzero sedimentation rate above and below the modeled region to avoid edge effects.

In this Bayesian inversion, the proposed model likelihood is evaluated only at each dated horizon. While the age of each model stratigraphic horizon is represented as a separate model variable, the ages of adjacent stratigraphic horizons are highly correlated so the problem is not underconstrained even when the number of model horizons grows very large. Gaussian prior distributions are imposed for depositional age (t) and hiatus duration (d), leading to a likelihood function following the form of the familiar Gaussian probability density function:

$$L(x,\mu,\sigma) = \frac{1}{\sqrt{(2\pi\sigma^2)}}\exp\left(\frac{-(x-\mu)^2}{2\sigma^2}\right)$$

Discarding the constant pre-exponential factor, (which will cancel in the likelihood ratio that is used to calculate acceptance probability) we may then write the log likelihood of the proposal evaluated against each dated stratigraphic horizon as

$$\mathrm{LL}_{\mathrm{prop\backslash dep}} = -\sum_{i=1}^{N_t}\frac{\left(t_{\mathrm{prop\backslash}i} - t_i\right)2}{2\sigma^2_{t\backslash i}}$$

where t_i and $\sigma_{t\,i}$ are the estimated age and uncertainty of each dated horizon i, and $t_{\mathrm{prop\ i}}$ is the proposed age for that horizon at a given step of the markov chain. Meanwhile, hiatuses are implemented as a minimum age difference between two model depth horizons; hiatus log likelihood is evaluated for each hiatus in the form

$$\mathrm{LL}_{\mathrm{prop\backslash hitatus}} = -\sum_{i=1}^{N_h}\frac{\max\left(d_i - d_{\mathrm{prop\backslash}i}, 0\right)^2}{2\sigma^2_{d\backslash i}}$$

where d_i is the estimated duration of a given hiatus. As such, there is no direct upper constraint on model hiatus duration. This limitation reflects the geological complication that hiatuses have no vertical thickness, so the duration of the 1 cm interval containing a hiatus is not equal to (and may substantially exceed) the duration of the hiatus alone. Consequently, we can effectively impose only minimum hiatus durations, with maximum hiatus durations constrained only indirectly by the quantitative geochronological constraints at dated horizons.

At each step of the Markov chain, the previous accepted (or initial) proposal is modified by randomly choosing a model horizon and perturbing the age-depth model with a symmetric Gaussian proposal distribution with standard deviation equal to the average analytical standard deviation. Any stratigraphic horizons that are out of superposition after this perturbation are assigned an age equal to that of the perturbed horizon, maintaining a monotonic age-depth relationship. Hiatus duration is thus adjusted only if the randomly chosen model horizon is directly above or below a hiatus. The likelihood of the proposal is then assessed both on the basis of hiatus duration and estimated depositional age of dated horizons

$$\mathrm{LL}_{\mathrm{prop}} = \mathrm{LL}_{\mathrm{prop\backslash dep}} + \mathrm{LL}_{prop\backslash hiatus}$$

and accepted or rejected on the basis of the summed log likelihood, with acceptance probability

$$P_{\mathrm{accept}} = \min\left(e^{\mathrm{LL}_{\mathrm{prop\backslash dep}} + \mathrm{LL}_{\mathrm{last}}}, 1\right)$$

in accordance with the Metropolis algorithm for a symmetric proposal distribution – a special case of the more general Metropolis-Hastings algorithm (Hastings, 1970).

Considering the large number of model horizons, and the limited number of horizons perturbed per proposal, we may see that adjacent steps of the Markov chain will be highly correlated, and that it may take on the order of 10,000 steps of the Markov chain to perturb the full depth range of the age-depth model. Consequently, the Markov chain undergoes a prolonged burn-in process, requiring ~4,000,000 steps to reach stationarity (Fig. S2). Once stationarity is achieved, the Markov chain gives a posterior estimate of the age distribution at each model horizon.

To be conservative, we discard the first 20,000,000 steps of the chain as burn-in. After this burn-in period, we collect 50,000 steps (in blocks of 25,000 to avoid memory limitations) of the stationary distribution sieved every 10,000 – that is, running for an additional 500,000,000 steps and collecting every 10,000$^{\mathrm{th}}$ step to the sieved output. Such sieving of the stationary distribution greatly reduces autocovariance and thus provides a more thorough sampling of the parameter space per model step saved.

In contrast to some other Bayesian age-depth models (Blaauw and Christen, 2011; Ramsey, 2008) our approach neither requires nor permits any prior assertions regarding the constancy, smoothness, or "memory" of sedimentation rate, since we do not consider such assertions geologically justifiable in siliciclastic sedimentary sections. In this way, our model bears some similarity to Bchron (Haslett and Parnell, 2008), though our approach to constructing and perturbing monotone age-depth proposals differs. Finally, due to the abundance of observed depositional hiatuses in the Koora Basin, our model has been architected to allow such hiatuses to be directly prescribed if their minimum duration can be independently determined. The importance of such hiatuses has been emphasized previously in the non-Bayesian age-depth modeling approach of Trauth (2014).

3. Results and discussion

3.1. Lithostratigraphy

Based on the macroscopic and microscopic core description we recognized 349 lithostratigraphic units in OLO12-1A, including the basal trachyte. Overall, the core is relatively fine-grained and includes input from both siliciclastic and volcaniclastic sources as well as lacustrine biogenic silicates (Fig. 4 and Table S5 show the results of semi-quantitative smear slide analysis). Of 345 distinct sedimentary units, silt (44%) and clay (20%) predominate based on proportion of total thickness. Siliciclastic silt and clay are mixed with varying amounts of diatomite, tuff, calcium carbonate, and zeolite. Relatively pure tuffs make up about 17% of the core. About half of the silt-grade sediment is diatomaceous, with pure diatomites making up only ~1% by thickness. Siliciclastic sand and gravel constitute 14% and 4%, respectively.

OLO12-1A documents multiple cycles of primarily lacustrine deposition with variable fluvial sediment input, including periodic influxes of volcaniclastics. The lacustrine deposits alternate with phases of lake regression and fluvial sedimentation, with pedogenic modification of the emergent sediments by subaerial surface processes. Pedogenically altered lacustrine sediments (i.e., paleosols) are in most cases directly overlain by unaltered lacustrine sediments and lack an intervening fluvial horizon. Increased volcaniclastic input recorded in the upper part of the core resulted in

thick packages of tephra deposited in lacustrine conditions, indicating that the Koora Basin depocenter maintained accommodation space during periods of rapid aggradation.

The most abundant microscopic components of the Koora sediments are in descending order volcanic glass, diatoms, calcite/aragonite crystals and clay particles (Fig. 4). The basal trachyte (recovered from 161.80 to 166.14 mbs) is directly overlain by diatomite as indicated by high proportions of diatoms (40–80%) between 161.50 and 159 mbs. From 161.50 to ~150 mbs phytoliths are very abundant (mostly 25–50%) and dominate the sediment from 155 to 150 mbs together with quartz/feldspars and clay. From 145 to 107 mbs diatoms are generally the most frequent sediment component (up to 100%) and together with sections rich in calcite/aragonite minerals (20–70%) form carbonaceous diatomite horizons from 135-130, at 120 and from 115 to 110 mbs. In this core interval tephra beds occur at 134, 131, 119, 118, 109 and 108 mbs. A thick package of pure tephra (100% glass) occurs at 106–101.2 mbs. Volcanic glass remains the most common sediment component from 100 to 50 mbs (up to <90%), with diatoms largely absent from 98 to 57 mbs, except for a pure diatomite layer at 65.75 mbs. A distinctive interval rich in zeolites occurs from 97.60 to 83.90 mbs, whereas calcite/aragonite rich horizons occur from 100-98, at ~81, ~77, ~75 and ~54 mbs. From 50 to 27 mbs, clay particles dominate the sediment, volcanic glass is consistently present but less abundant than below, and diatoms are particularly common between 45 and 40 mbs.

3.2. Paleosol characterization and estimation of hiatuses

Thirty hiatuses are recognized in OLO12-1A, identified by the presence of weakly to moderately developed paleosols (Table S4). The paleosols can be classified using USDA Soil Taxonomy as paleo-Entisols, -Inceptisols, and –Vertisols (Staff, 2014). Entisols are very weakly developed soils with little or no evidence of soil horizons, and often contain relict bedding. Inceptisols are more strongly developed than Entisols with soil horizonation and ped formation, but lack distinguishing features that would allow them to be classified as another soil order. Vertisols are clay-rich soils with cracks, pedogenic slickensides, and other vertic features that form as a result of shrinking and swelling of clays during wetting and drying. The paleosols represent times of subaerial exposure, and their frequency through the core indicates multiple depositional transitions, from intervals of aggradation (usually lacustrine) to intervals of temporary land surface stability and soil formation.

3.3. Compensating for variable depositional rates (z-prime depth)

Applying the rules for sediment compression described above (section 2.5), 137 of 349 lithological units were compressed (34 by 70%, 39 by 90%, and 64 by 100%; Table S6). The cumulative compression of core OLO12-1A was 31.43 m, thus the original drilled-depth of the core of 166.14 m was transformed to 134.71 m (Fig. 5). Diatomite was unaffected, but other major lithological types (clay, silt, tuff, sand, and gravel) were reduced in thickness; tuff was reduced the most (16.1 m), followed by sand (6.5 m).

Most of the depth compression (>97%) was applied to lithological units between 27 and 106 mbs due to the abundance of tephra in this part of the core (Fig. 6). From the base at 166 mbs–106 mbs a total compression of only 0.87 m was applied, affecting a 0.5 m thick pumiceous tuff at 152 mbs and six intervals of drilling fluid injection (Fig. 6). Above 106 mbs, compression was mostly applied to seven intervals of core between 1.5 and 7.5 m thick. These included five massive tuffaceous beds (at 106-101.2, 82.5-77.3, 72.8-66, 65.7-58.8 and 53.8–52.4 mbs) with 70–100% volcanic glass; one subaqueous tuffaceous debris flow at 97.8–95.1 mbs; and a silty, pumiceous-sandy clay at 47.6–45.6 mbs. The remaining compressed core intervals were less than one meter thick and consisted of beds of vitric tuff, pumice or sand as well as drilling fluid injections.

3.4. Volcanic event stratigraphy

Table S7 details the volcanic event deposits identified in the core. These are considered to be derived from eruptive episodes that occurred shortly before the time of deposition (i.e., within several tens to hundreds of years). A total of 111 events were observed, ranging in thickness from less than a millimeter to 10.67 m. Pumice was observed in 62 of these events, concentrated in the upper half of the core, with only two pumiceous events older than 400 ka. Several important caveats must be noted, in that errors

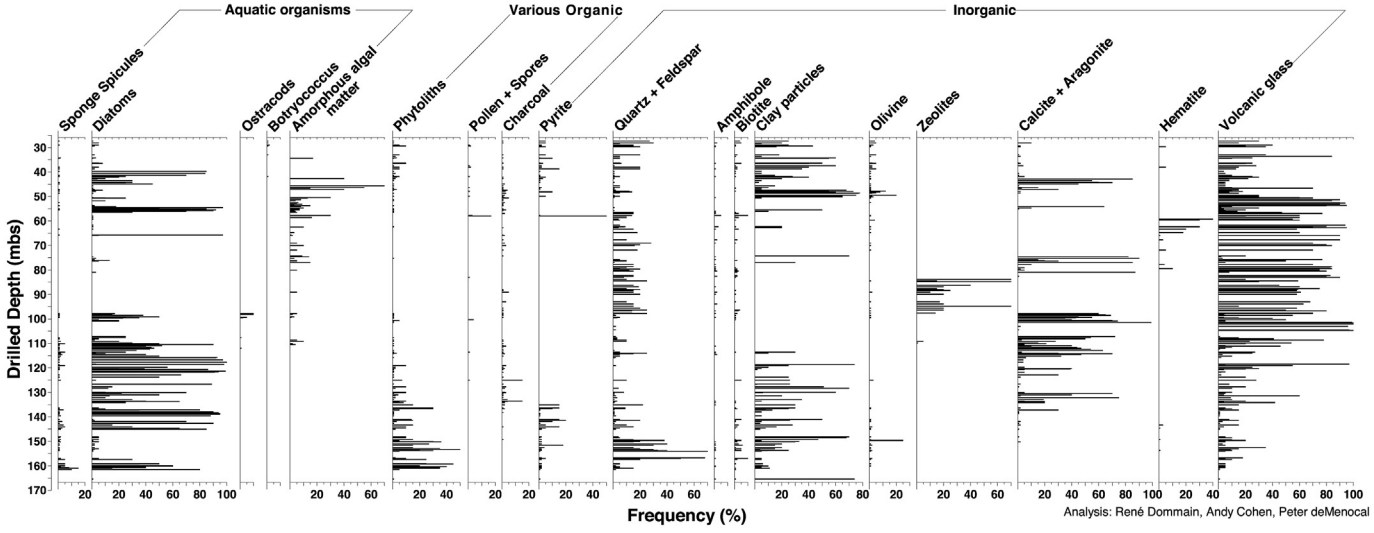

Fig. 4. Frequency of components in OLO12-1A smear-slide analysis. The most abundant microscopic components of the Koora sediments are in descending order volcanic glass (dominating the upper half of the core), diatoms (in the lower half and intermittently in the upper fourth), calcite/aragonite crystals (sporadically through the core) and clay particles (concentrated in the lower and upper thirds of the core).

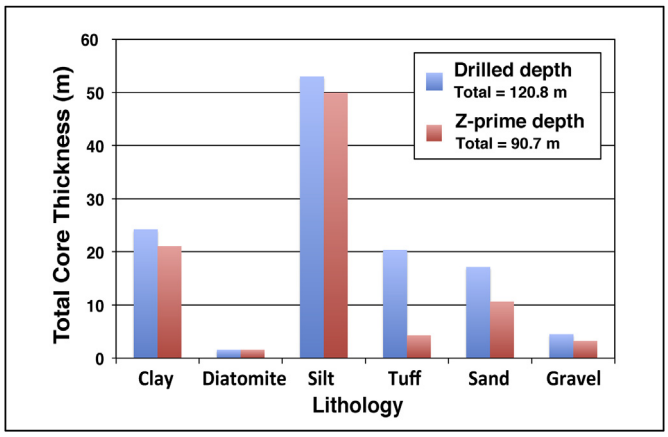

Fig. 5. Comparison of total thickness of clay, diatomite, silt, tuff, sand, and gravel in converting from drilled-to z-prime depth. Diatomite was unaffected, but other major lithological types (clay, silt, tuff, sand, and gravel) were reduced in thickness; tuff was reduced the most, followed by sand.

in the volcanic event stratigraphy are most likely in the form of 1) merger of multiple events into a single event observation; 2) omission of events that escaped detection due to small volume or extreme dilution by sediment; and 3) delayed detection of volcanic events due to potentially extended residence time in fluvial systems. In regard to the last point, however, it should be noted that only a few beds in the upper part of the core were observed to be too old for their stratigraphic position at the 95% confidence level (see below; also identified in Tables 1 and S7).

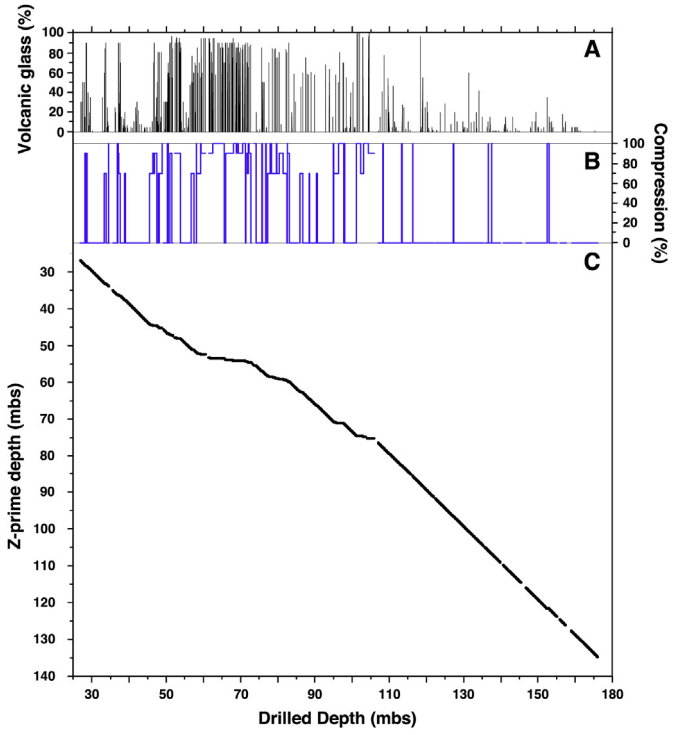

Fig. 6. Z-prime depth compression as a function of depth in the core. A) Percent volcanic glass shards in smear-slide analysis. B) Degree of compression assigned to drilled-depth intervals. Gaps in the series denote lost core. C) Correspondence of drilled- and z-prime depth measures. Compression rules were applied based on the amount of volcanic glass observed: >60%–75% glass = 70% compression; 75–90% = 90% compression; and >90% = 100% compression (i.e., removed). Most of the depth compression (>97%) was applied to lithological units between 27 and 106 mbs due to the abundance of tephra in this part of the core.

3.5. $^{40}Ar/^{39}Ar$ dating

Single-crystal incremental heating of K-feldspar phenocrysts from tephra horizons, and from the basal trachyte flow, yielded 22 new $^{40}Ar/^{39}Ar$ ages calibrating OLO12-1A (Table 1). Age-probability density spectra for the dated units are illustrated in Fig. S3.

The basal trachyte gave an age of 1.0837 ± 0.0040 Ma, indistinguishable at the 95% confidence level from the age of the basal trachyte in the HSPDP Lake Magadi core 16 km to the southwest (1.0783–0.0036 ka; Owen et al., 2018), suggesting that these belong to the same fissure flood eruptive sequence. Based on mode of emplacement, large K-feldspar phyric mineralogy, age, and widespread mapped distribution, these rocks are attributed to the peralkaline trachyte and pantellerite flows of the Magadi trachyte series (Baker and Mitchell, 1976; Guth and Wood, 2013). These dates are also indistinguishable from an age obtained from the late-stage pyroclastic apron west of the adjacent Ol Doinyo Nyokie rhyolitic center (1.065–0.014 Ma; Deino and Potts, 1990), suggesting that this vent may be a differentiate of the Magadi Trachyte magma.

Most dated tephra samples are from the middle third of the core, but extend as deep as 152.63 m (out of 166 m total depth to basement), and as high as 28.50 mbs (note that the upper 27 m of the core was augured and not sampled for $^{40}Ar/^{39}Ar$ dating). Analytical uncertainties assigned to the mean ages had a median value of 0.9% 1σ (range 0.3–4.7%); two dated units represented by just two grains in the lower part of the core just above the BMB had the highest uncertainty (4.2–4.7%); fortunately, as shown in Section 3.6, the BMB provides excellent age control in this portion of the core. While most of the tephra ages fall within stratigraphic order at the 95% confidence level, three beds in the upper 50 m of the core yield ages that are too old (Table 1); the largest deviation is ~20 ka from the Bayesian stratigraphic age model (sample 'OLO12-1A-37Q-1 60–67'; Table 1).

3.6. Magnetostratigraphy

The ChRM declination, inclination and MAD values were plotted versus depth in order to identify any possible reversal boundaries (Fig. 7). The MAD values are all less than 10° (all but three are <7°) and, considering that a minimum of six demagnetization steps were used in the calculation of the ChRM, indicate that all of the samples produced quality ChRM directions. The inclination values are generally negative, but within the expected range of the geocentric axial dipole predicted for the site latitude (−3.2°). Considering that paleomagnetic secular variability (PSV) can be as high as ± 20–30°, and given the near-equatorial location of the site, inclination values are expected to be low and likely cross the geomagnetic equator due to PSV. Inclination values therefore prove inadequate for identifying possible geomagnetic field reversals. Conversely, the changes in declination associated with a field reversal would result in a near 180° change in declination values across the reversal boundary. The declination data shows large changes at ~153.08, 153.8 and 160.5 mbs (Fig. 7), but it is clear that the change at 153.8 mbs is at core section break and therefore is likely reflecting sampling of a different plane. The change at 160.5 mbs appears to be associated with a decreasing trend in declination values that resulted in a zero-crossing, a common artifact in rotational drilling. The change at 153.08 mbs appears to be a true reversal as it lies within a single core section and there is no apparent linear trend in the adjacent data. The change in declination values across the reversal is ~160° and is observed in 2 samples (153.03 and 153.08 mbs; Fig. 7). Based on the position of

the samples, it appears that a geomagnetic reversal occurred between 153.08 and 153.15 mbs. Considering the stratigraphic position of this reversal relative to the radiometric age constraints presented herein, this reversal is attributed to the BMB.

3.7. Bayesian age modeling

Table 1 lists the chronostratigraphic control points input to the Bayesian stratigraphic age model, including 22 $^{40}Ar/^{39}Ar$ ages on tephra beds and on the basal trachyte lava, the age of the BMB (781.0 ± 0.3 ka (Ogg et al., 2012), and an estimate of the modern age of the surface at the top of the core (50 ± 50 y). Two depth scales, actual mbs (drilled depth) and z-prime depth, are given for each control point. Table S4 is a tabulation of recognized paleosols with their estimated hiatus duration and error, which also serves as constraints to the age model.

The age models calculated using the methods and data described are provided in Table S8 for the Bayesian model using drilled depths and without hiatuses (calculated at a 22 cm depth interval), and the final model using z-prime depth and incorporating hiatuses in Table S9 (calculated at a 1 cm interval). Fig. 8 shows that the overall shape of the depth vs. age relationship of the two models is similar, characterized by initially relatively slow average sediment accumulation rates in the lowest fourth of the core from ~1 Ma to ~400 ka, followed by increasingly rapid accumulation to ~200 ka (50 m depth). Sediment accumulation rates slow again from ~200 to 100 ka, then finally rise to the top of the core. In the range where the model is applied to core proxy studies (below the augured level at 27 mbs), uncertainties in the age of the model predictions range from 0.4 to 19% at the 95% confidence interval for both the drilled-depth and z-prime depth models. The greatest uncertainties are at the upper and lower ends of the models, in the ~1080–500 ka and 100–0 ka intervals.

Fig. 7. ChRM declination, inclination and MAD values plotted against depth. Solid and dashed horizontal lines indicate core breaks and core section breaks, respectively. Vertical solid line indicates the geocentric axial dipole predicted inclination value (−3.2°) for the site latitude. The ~160° declination change at 153.08 mbs represents an actual reversal and not a drilling artifact. Based on the position of the samples, it appears that a geomagnetic reversal occurred between 153.08 and 153.15 mbs, attributed to the BMB.

Fig. 9 show the instantaneous sediment accumulation rate derived during the Bayesian model construction for both the drilled- (Fig. 9A) and z-prime (Fig. 9B) depths. Labeled rate intervals A–D in both models are consistently low (<10 cm/ka), but jump abruptly at the D/E boundary (~400 ka) to ~20 cm/ka, coincident with a major uptick in volcanism (evident in the increase in volcanic glass shard percentage in thin section, and sudden high frequency emplacement of volcanic event deposits). This transition occurs at roughly the mid-point of the interval of major erosion at Olorgesailie, thus was not foreseen by prior outcrop studies. Accumulation rates reach maximum levels in interval F from ~400 to 190 ka to ~30–380 cm/ka for drilled-depth and ~20–230 cm/ka for z-prime depth, due to the influx of voluminous pyroclastic tephra. In interval G (190–100 ka), sedimentation rates (~10 cm/ka) drop to near pre-400 ka levels. Interval H represents a sharp spike in rate due to volcanic input (maximum rate ~150 cm/ka for drilled-depth, and ~90 cm/ka for z-prime depth), followed by a final high sedimentation rate interval (I) to the surface. Note, however, that this uppermost portion of the model is speculative, in that the there is no chronostratigraphic control in this augured interval, and we are forced to assume an age for the modern surface (~50 ± 50 y). The success of the z-prime depth transformation in smoothing sedimentation accumulation rates by compressing events is demonstrated by the more subdued peaks in sedimentation rate evidenced in intervals F and H.

4. Discussion

The Quaternary evolution of the Kenya Rift was controlled by the interrelated dynamics of extensional faulting and volcanism. Intra-rift faulting in the south Kenya Rift led to the fragmentation of the rift floor into pronounced horst-graben topography with resulting basin compartmentalization (Baker, 1986) and variable patterns of sedimentary infilling. In addition, intra-rift volcanism led to the formation of many Pleistocene volcanic centers and frequent eruptions (Robertson et al., 2016). Growth of volcanoes altered drainage patterns, while dispersal of voluminous pyroclastic material from repeated eruptions contributed to basin infilling. These volcano-tectonic dynamics altered basin morphology, landscape hydrology and sediment influx and therefore affected the sedimentary environment of the southern Kenya Rift, leading to rift-floor basins characterized by laterally variable sedimentary facies (Baker, 1986). OLO12-1A provides an opportunity to document these landscape dynamics, but its complex sedimentary sequence poses a major problem for conventional age-depth modeling. Simple age interpolation between radiometric dates is inappropriate for a heterogeneous core such as this, particularly when the ultimate goal of the exercise is to facilitate the construction of highly resolved and temporally accurate environmental proxy records. The varied lithologies, numerous unconformities expressed as paleosols, and the concave age-depth curve demonstrating intensifying rates of sediment accumulation over time, require a circumspect approach to generating a robust age model.

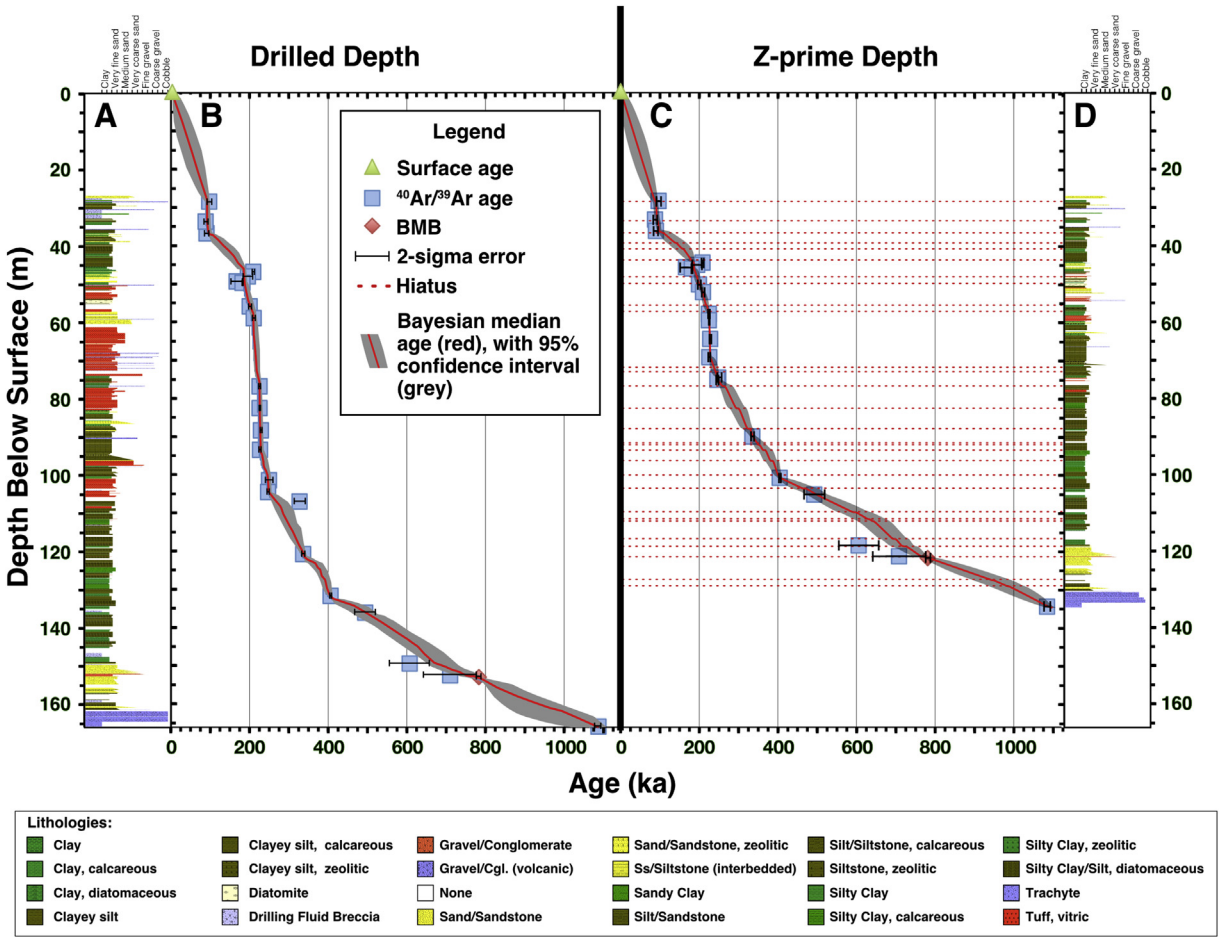

Fig. 8. OLO12-1A stratigraphic columns, chronostratigraphic control points, and age models, expressed on drilled- and z-prime depth measures. A) Stratigraphic column using drilled depths. Key to lithologies is provided below the graphs. B) Location and error of chronostratigraphic control points, and the Bayesian stratigraphic age model, expressed as drilled-depths. C) Same as previous panel, but expressed on a z-prime depth axis, and showing stratigraphic position of hiatuses included in the model. D) Stratigraphic column using z-prime depths. The general shape of the depth vs. age relationship of the two models is similar, characterized by initially relatively slow average sediment accumulation rates in the lowest fourth of the core from ~1 Ma to ~400 ka, followed by increasingly rapid accumulation to ~200 ka (50 m depth). Sediment accumulation rates slow again from ~200 to 100 ka, then finally rise to the top of the core.

4.1. Sedimentation patterns

OLO12-1A exhibits sedimentation patterns ranging from intervals of non-deposition (i.e., hiatuses) evidenced by numerous paleosols, to pulses of high sediment accumulation associated with the influx of thick tephra depositonal events. Overall, the age-depth model exhibits a general increase in sediment accumulation rates over time (Figs. 8 and 9).

The oldest part of the core (166–131 mbs; ~1084–400 ka) is characterized by the lowest rates of sediment accumulation, reflecting limited accommodation space in the depositional sump combined with slowly deposited diatomaceous and clayey sediments, a scarcity of volcanic material, possible local erosion by fluvial processes, and hiatuses recorded by 11 paleosols (Table S4). These paleosols together encompass approximately 30 ka and include five of the longest paleosol phases (~5 ka duration) in OLO12-1A. This basal 35 m of the core was deposited over a period of ~680 ka.

The succeeding 25 m of core from 131 to 106 mbs (~400–260 ka) shows a slight increase in average sediment accumulation rate (Fig. 8), with primarily lacustrine deposition interrupted by periods of emergence recorded in seven paleosols together representing ~26 ka (Table S4). Carbonate muds and volcanic glass increase in abundance, while siliciclastic sand and other evidence of fluvial activity is minimal. In total, the basal 60 m of core required over 820 ka to accumulate, due to multiple long periods of pedogenesis and slow sedimentation.

In contrast, strong pulses of volcanic input from 106 to 50 mbs (~260–187 ka), as well as background lacustrine sedimentation and six short paleosol phases (totaling just 1.4 ka) (Table S4), led to the deposition of 56 m of sediment (40% of the recovered core) in only ~73 ka. This interval is characterized by an order-of-magnitude higher accumulation rate than previously, and exhibits a maximum rate of ~380 cm/ka at ~225 ka (Fig. 9).

Deposition dominated by biogenic silica and authigenic carbonates, four phases of soil formation (together = 2.5 ka) and diminished tephra input led to reduced sediment accumulation from 50 to 37 mbs (187-100 ka). Finally, renewed influx of large volumes of volcanic material from 37 to 27 mbs (100-80 ka) resulted in another peak in sediment accumulation rate (interval H of Fig. 9), despite two 0.75 ka long paleosols phases.

4.2. Age-model construction

Allochthonous volcaniclastic sediment influx and paleosol formation strongly influenced the Koora Basin stratigraphy, beyond

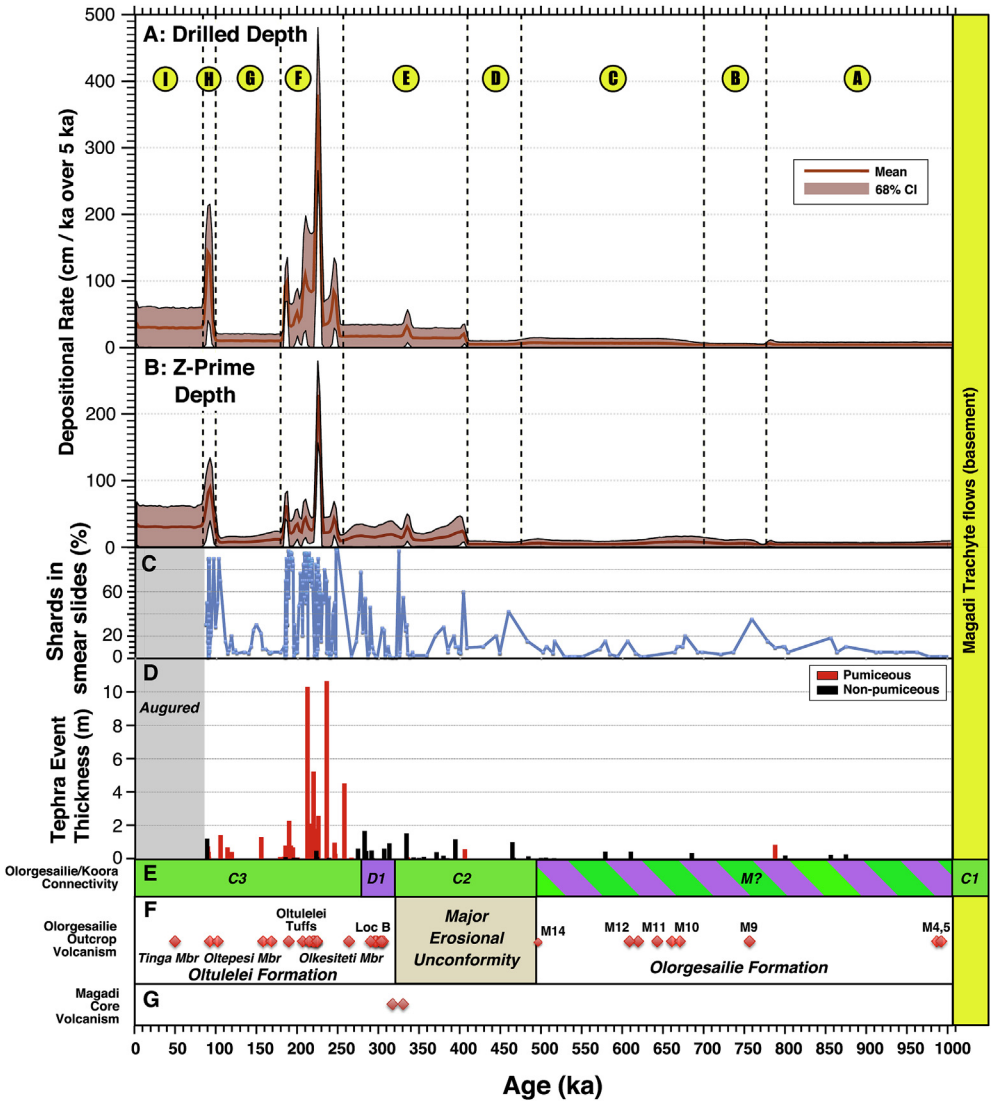

Fig. 9. Depositional rates, volcanic events, and comparative basin history. (A) Depositional rates derived from the drilled-depth Bayesian age model using a 5 ka sliding window. Major changes in rate are marked by vertical dashed lines and labeled A–I for reference. (B) Depositional rates using the z-prime depth conversion. (C) Percentage of volcanic glass shards in smear-slide analysis. (D) Volcanic tephra event deposits inferred from core images, ICD lithologic descriptions and smear slide analysis (red = pumiceous, black = non-pumiceous). (E) Conjectured timing of connectivity between the Koora and Olorgesailie Basins through the Koora Graben based on the volcaniclastic record (green color = connected, purple = disconnected, green/purple striped = mixed or uncertain). 'C1', 'C2', and 'C3' are episodes when the basins are connected, from oldest to youngest; 'D1' is an interval when the basins are separated. The interval labeled 'M?' is mixed or uncertain. (F) Age of major pyroclastic deposits at Olorgesailie (all are pumiceous). 'M4' through 'M14' are members of the Olorgesailie Formation. 'Loc B' are coarse pumiceous tuffs within the lower Olkesiteti Member of the Oltulelei Formation at Locality B (Deino et al., 2018). (G) Magadi core pyroclastic volcanism. Yellow bar on the right represents the Magadi flood trachyte emplacement event common to all three basins. (For interpretation of the references to color in this figure legend, the reader is referred to the Web version of this article.)

background lacustrine and clastic sediment deposition. The first task in establishing an age model of the core was to examine lithologic units for tephra abundance and apply a compression factor as necessary based on established rules. In doing so we generated a compressed core-depth scale termed 'z-prime,' which resulted in a 20% thickness adjustment relative to the original core length (Fig. 5). The z-prime scale exhibits reduced sediment accumulation rates in volcanic-rich intervals, as expected (Figs. 8 and 9). For instance, after applying our compression factors to the highly tuffaceous interval from 106 to 50 mbs, its thickness is reduced to 28.5 m and the average sedimentation rates are lowered by ~50%. Without attention to variable sedimentation rates, the duration of tephra deposition would be exaggerated compared to deposition of biogenic silica, carbonates or other primary lacustrine sediments.

Recognition of extensive paleosol formation in the core stratigraphy necessitated the incorporation of hiatuses into the age model, positioned at the top of each paleosol, with a duration for each estimated between 50 and 5000 y based on a paleosol maturity index (Tables S3 and S4). The effect on the age model is to introduce a sharp change in age at the top of the hiatus, with centimeter resolution (Figs. 2 and 8c). Sediment accumulation rates increase before and after a hiatus (Fig. 2). Ignoring hiatuses related to subaerial exposure and soil formation in reconstructions of lake basin histories would result in the recognition of only a single lake phase, while overlooking dry episodes. Assuming that hiatuses are accommodated by age interpolation would give an incorrect impression of a continuously aggrading system and minimize the dynamics of lake-land transitions, thus masking the potentially complex hydroclimatic history of a region. For example, OLO12-1A exhibits multiple unconformities where paleosol surfaces are

directly overlain by diatomites (Fig. 3), providing important examples of abruptly changing moisture conditions and likely rapid flooding of a dry land surface, rather than a slow increase in groundwater table and runoff. An age model incorporating prescribed hiatuses can be used to identify the timing of significant changes in moisture supply. Failure to incorporate hiatuses also leads to inaccurate relative age relationships between lacustrine proxies (e.g., diatom assemblages) and soil-based proxies (e.g., pedogenic soil carbonates) that are co-located with depth but deposited at different times. As illustrated in Fig. 10, diatom assemblages deposited within primary lacustrine sediments and used to reconstruct lake depth are commonly found in OLO12-1A at the same centimeter depth as pedogenic soil carbonates that formed within primary lacustrine sediment during subsequent periods of subaerial exposure. Without incorporating hiatuses, the same modeled age is generated for co-located lacustrine and soil-based proxies, yielding artificially younger modeled ages for lacustrine proxies and older for soil-based proxies (Fig. 10a). By incorporating hiatuses, modeled ages for lacustrine proxies no longer coincide with periods of subaerial exposure and the proper relative age relationship between lacustrine and soil-based proxies is retained (Fig. 10b). Ultimately, identifying paleosols in sediment cores and adding their estimated duration leads to more precise environmental reconstructions and better age models. This new protocol for generating age-depth stratigraphic models may be appropriate for cores from many other dynamic sedimentary basins, in particular from the EARS or other magmatic rifts.

4.3. *Volcanic record of the Koora Basin*

Volcanism is an inherent feature of rifting and plate segmentation in the magmatically active EARS (e.g., Robertson et al., 2016; Wright et al., 2006). Pleistocene volcanism strongly influenced Koora Basin development first by establishing essentially a broad volcanic tableland following regional emplacement of Magadi Trachyte flows, and then by supplying varying rates of pyroclastic material over the past 1 Ma to help bury these flows under >100 m of sedimentary strata. In terms of microscopic sediment composition, volcanic ash is in fact the most abundant component (~30%) of the core, more prevalent than lacustrine diatoms or authigenic carbonates (Fig. 5). The sedimentary composition of the Koora Basin differs from that of the Olorgesailie Basin (Isaac, 1977; Behrensmeyer et al., 2002, 2018) and the adjacent Magadi Basin (Owen et al., 2018) because of the dominance of volcaniclastics in the Koora Basin. This highlights the depositional and stratigraphic spatial heterogeneity of adjacent basins within the southern Kenya Rift (Baker, 1986).

The formation of Pleistocene intra-rift volcanoes and the associated buildup of relief, in particular the rise of Mt. Suswa since 400 ka (Baker, 1986), likely influenced the drainage network and catchment of the Koora Basin (Fig. 1). Rerouting of rivers and changes in catchment configuration may have contributed to the observed abrupt shifts toward higher sediment accumulation rates and associated deposition of fluvially transported tuff (Behrensmeyer et al., 2018).

Analysis of volcanic event deposits in OLO12-1A provides insight into the character and distribution of volcanism in the southern Kenya Rift over the past million years, as well as hints regarding connectivity of the Koora Basin with the Olorgesailie Basin to the north, and the Magadi basin to the west (Table S7; Fig. 9). The initial 600 ka of the core record exhibits more or less randomly spaced, relatively low volume, non-pumiceous ash deposits up to 2 m thick at the comparatively slow pace of ~31 events/Ma. The smear-slide record shows increasing volcanic input beginning ~500 ka (Figs. 5 and 8), and at ~400 ka, the pace of volcanism increases dramatically to ~270 events/Ma with maximum thicknesses to ~10.7 m. The greatest volume and accumulation rate of tephra is recorded after ~300 ka, with almost all pumiceous deposits being recognized in the last 270 ka. Pyroclastic deposition is particularly intense between 260 and 210 ka. An important change is recorded in the character of tephra deposits at ~270 ka that lags the upswing in volcanism by 130 ka; prior to 270 ka virtually all tephra are restricted to ash particle size (<2 mm; with the exception of a significant pumiceous tephra at ~788 ka), whereas subsequently almost all events contain pumice. This time lag could represent a change in the nature of the volcanic eruptions, in volcanic source areas, in the drainage network, or in the capacity of the fluvial system to transport pumice from source areas to the Koora Basin, including temporary storage in the Olorgesailie Basin. Trapping of pumice in the northern basin is evident from ~320 to 270 ka (D1 interval, Fig. 9E), given their abundant presence in the Oltulelei Fm. within coarse cut-and-fill channels at this time (Behrensmeyer et al., 2018; Deino et al., 2018) but they are notably absent from the core.

To understand the significance of these volcanic depositional patterns, it is important to review the location and age of likely volcanic sources of the OLO12-1A tephra. Three major potential source areas exhibited extensive pyroclastic volcanism either shortly before or during the last 1 Ma: Ol Doinyo Nyokie, the Ngorongoro Volcanic Highlands (NVH), and a cluster of five volcanoes or vent areas in the Central Kenya Rift near Lake Naivasha, known as the central Kenya peralkaline province (Fig. 1) (CKPP; Macdonald and Scaillet, 2006).

The Ol Doinyo Nyokie dome ignimbrite complex (Baker, 1975) lies just 1.5 km SE of the drill site. Coarse pumice tuffs attributed to the late stage of activity of this center (Baker, 1975) have been dated at 1.065 ± 0.014 Ma (Deino and Potts, 1990). Considering that lava flows forming the basement of OLO12-1A are almost the same age (1.0837 ± 0.004 Ma), it is apparent that most activity at Ol Doinyo Nyokie ceased prior to the initial phases of sedimentation at the drill site. Even fluvially derived volcaniclastics from this nearby volcano appear to be absent from the core record. It is possible, however, that ash deposits, particularly in the earliest part of the core, were erupted during waning activity of this center. Ongoing geochemical analysis of tephra deposits from the core and potential source areas may resolve this question.

A second major potential source area for pyroclastic deposits in OLO12-1A is the NVH, ~130 km to the southwest in northern Tanzania (Fig. 1). The nepheline carbonatite volcanoes of Embagai, Kerimasi, and Ol Doinyo Lengai in the northwestern NVH were all active during the past million years (Foster et al., 1997; Mollel and Swisher, 2012; Sherrod et al., 2013; Mana et al., 2015); however, the magma chemistry of these centers is generally incompatible with the feldspar-phyric silicic ashes identified in the core. There are exceptions, however; for example, a K-feldspar phyric phonolite lava exposed on the southeastern flank of Ol Doinyo Lengai has been dated at 338 ± 23 ka (Sherrod et al., 2013). Additionally, isolated deposits of near-vent, K-feldspar bearing siliceous pumiceous tephra have recently been discovered in the NVH with ages in the range of ~700–200 ka (AD, unpublished data). Tephra from these eruptions may have reached the Koora Basin as fallout (likely in the ash size range) rather than fluvial transport, given the presumed early segregation of the Koora and Natron-Magadi Basins due to faulting. Also, in northern Tanzania, though outside the NVH, Mt. Meru was active in the last 500 ka (Mana et al., 2015), but is much further from the Koora Basin than the other centers (~170 km to the southeast of OLO12-1A; Fig. 1).

Rather than Ol Doinyo Nyokie and the NVH, the central Kenya peralkaline province (CKPP) is likely the predominant source of at least the voluminous, coarse, pumiceous tephra in the last ~270 ka

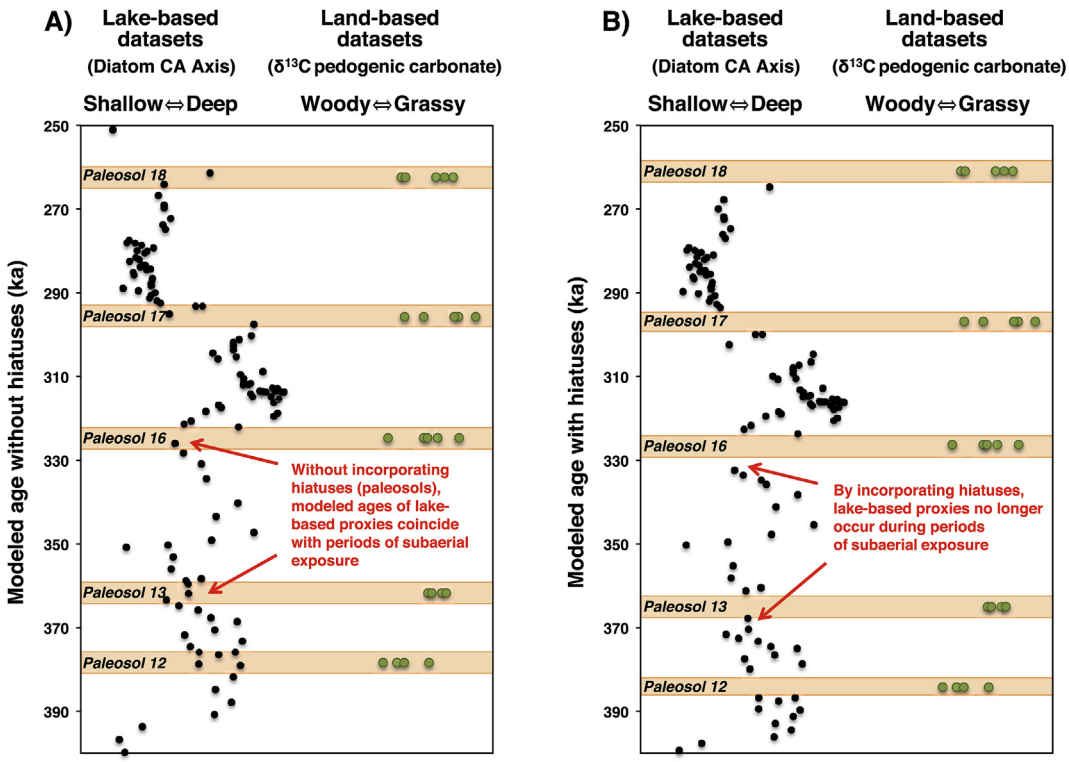

Fig. 10. Schematic of modeled ages of lacustrine and soil-based proxies (A) without and (B) with incorporation of hiatuses in lacustrine sediment deposition due to subaerial exposure and soil formation. Width of orange bars represent estimated and modeled hiatus durations in panels (A) and (B), respectfully, given in Table S4. Carbon isotopes of pedogenic carbonates are shown at the mid-point of hiatus durations. Without incorporating hiatuses, the same modeled age is generated for co-located lacustrine and soil-based proxies, yielding artificially younger modeled ages for lacustrine proxies and older for soil-based proxies. By incorporating hiatuses, modeled ages for lacustrine proxies no longer coincide with periods of subaerial exposure and the proper relative age relationship between lacustrine and soil-based proxies is obtained. (For interpretation of the references to color in this figure legend, the reader is referred to the Web version of this article.)

record of OLO12-1A, based on considerations of rift morphology, drainage patterns, volcanic history of the CKPP, and outcrop tephra accumulations at Olorgesailie. The CKPP, which includes the large, mid-Pleistocene to Recent silicic centers of Menengai, Eburru, Olkaria, Longonot, and Suswa, lies ~80–130 km the north in the Central Kenya Rift (Fig. 1) (Macdonald and Scaillet, 2006). Three of the CKPP volcanoes, Olkaria, Longonot and Suswa, are located in the present catchment of the Koora Basin (Fig. 1) and drainage patterns provide a direct fluvial transport pathway for volcaniclastic materials from south of the Naivasha basin to the drill site via the Kedong depression, Enkobirri Gorge, Olorgesailie Basin, Koora Graben, and finally into the Koora Basin (Baker and Mitchell, 1976; Behrensmeyer et al., 2018). Especially noteworthy in this regard are the voluminous coarse pumiceous tephra accumulations in OLO12-1A from ~258 to 187 ka, which encompass the interval of the similarly voluminous multiple pumiceous tephra beds of the Oltulelei Tuff (~225–190 ka) of the Olorgesailie Basin outcrop record (Behrensmeyer et al., 2018; Deino et al., 2018).

The CKPP may also be the dominant source of earlier (~1000–400 ka), primarily non-pumiceous tephra in OLO12-1A. Older K-feldspars encountered during the core $^{40}Ar/^{39}Ar$ single-crystal dating effort, presumably mainly detrital contaminants, have similar age groups in pre- and post-400 ka core levels (Fig. 11), suggesting they may have shared the same drainage systems. However, coarse tephra are sparse before 400 ka in the core, while abundant in the Olorgesailie outcrop record (Fig. 9). This difference may be the result of preferential sediment trapping in the Olorgesailie Basin or the northern Koora Basin, or indicate that the Olorgesailie Basin did not drain directly into the Koora Basin throughout much of the first half of the core history. Differences in population density in the three main detrital age groups between the pre- and post-400 ka data sets may speculatively reflect variability in vegetation cover and erosion in the source areas accompanying climate change, though a detailed detrital provenance study would be needed to examine this hypothesis.

The new age model provides a precise foundation for placing the lithostratigraphy of the core in a temporal framework. Sedimentation began soon after emplacement of Magadi Trachyte (1.0837 ± 0.0040 Ma), with low input of volcaniclastic material during a period of lacustrine and subaerial deposition between ~1100 and 500 ka (Phases A–C; Fig. 9). During this interval, lacustrine diatomites and distinctive, typically pumiceous tephra units alternated with intervals of paleosol development in the Olorgesailie Basin to the north. The different patterns of deposition in this time interval suggest the absence of a direct fluvial connectivity between the two basins. However, this inference applies only to the lacustrine and tephra depositional phases of the Olorgesailie basin as it is not possible to assess connectivity during subaerial phases represented by the northern basin paleosols. Also, these relationships do not exclude intermittent connectivity via a narrow neck in the Koora Graben as might be enabled by lake highstands; for example, outcrop of pumiceous tuff correlated to tephra in diatomaceous Olorgesailie Member 12 has been found in the northern Koora Basin, indicating a lacustrine connection at ~609 ka (Deino and Potts, 1990). Predominantly lacustrine facies in both areas between 600 and 500 ka suggest a shared interval of high lake level, whether or not there was a connection via the Koora Graben. Restricted or absent connection between the basins is indicated by the lack of similar-age tephra, however, and this lasted at least until the period of northern basin erosion between ~500 and 320 ka

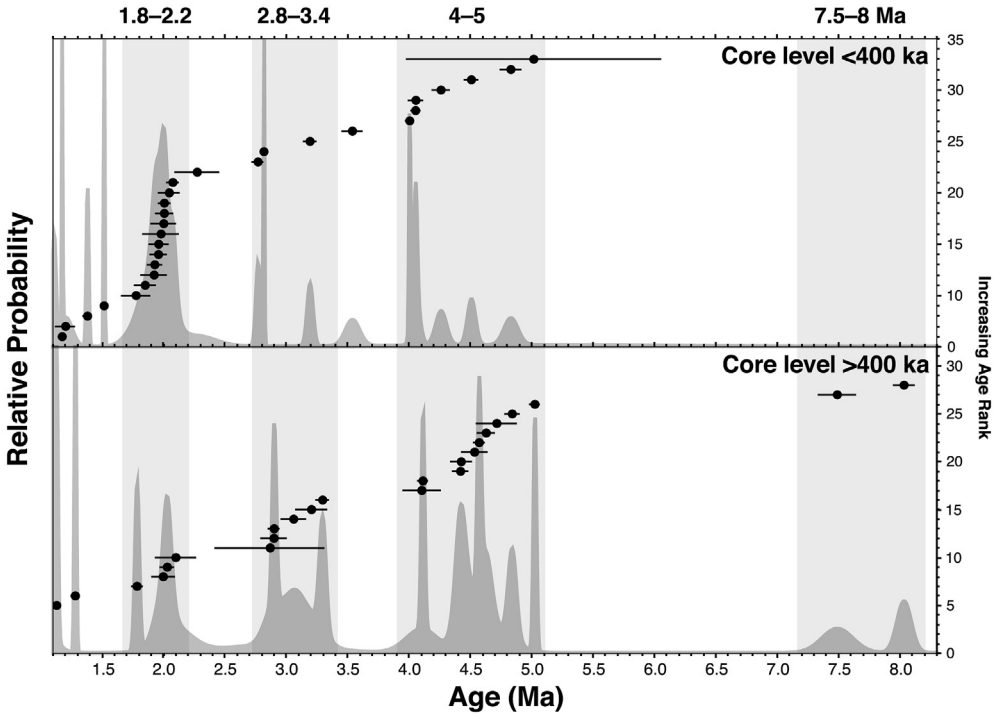

Fig. 11. Age-probability density spectra for older xenocrystic contaminants encountered during $^{40}Ar/^{39}Ar$ dating of the core tephra, interpreted to be dominantly detrital contaminants introduced during fluvial transport. The two panels divide the core into pre- and post-400 ka sampling levels. Four prominent age groups are recognizable: 7.5–8, 4–5, 2.8–3.4, and 1.8–2.2 Ma. The three younger groups are present in both spectra. The oldest group is seen in only the older levels of the core, but only two grains were encountered, thus the difference between the levels may not be significant.

(Phase D, early E). In the Koora Basin, this prominent erosional phase coincided with alternating lacustrine sedimentation and paleosol development plus increasing tephra input. Although there is no clear evidence in OLO12-1A of large amounts of eroded sediment entering the Koora Basin from the north, we propose that a fluvial drainage system connected the basins at this time since the Koora Basin is the only reasonable depocenter for the large volume of material removed from Olorgesailie, given geographic constraints. A renewed phase of basin independence is indicated by the occurrence of unique tephra at ~300 ka in the north (Locality B) (Fig. 9E; D1 toward the end of Phase E). This changed with an influx of large amounts of tephra beginning ~270 ka, which overfilled the northern basin and spread southward into the Koora Basin, where a thick volcaniclastic sequence was deposited in a moderately deep lake. This scenario recurred intermittently until ~170 ka (Phase F). The two basins thus were hydrologically connected after ~270 ka, with an additional pulse of tephra deposited at ~100 ka (Phases G, H). Correlations and non-correlations of the tephra in these two records provide an initial, in part speculative, reconstruction of basin connectivity that will be further tested with additional data from OLO12-1A sedimentology, geochemistry and paleontology.

The comparative volcanic depositional patterns between the Koora Basin and the Magadi Basin to the west is less informative, because there is just one recognized coarse pyroclastic sequence in the Magadi core, dated by the $^{40}Ar/^{39}Ar$ technique at ~330–316 ka (Owen et al., 2018). This is a thick (~5 m) siliceous pumice tephra sequence that has no match to the Koora Basin record; thus it appears unlikely that the adjacent basins were connected at this time. The Koora and Magadi basins were presumably part of an integrated low-relief landscape after regional emplacement of the Magadi Trachyte flood lavas just prior to 1 Ma, but were separated, perhaps soon thereafter, by tectonism resulting in the emergence of the intervening horst.

5. Conclusion

The Olorgesailie Drilling Project and the related HSPDP in East Africa were initiated to test hypotheses and models linking environmental change to hominin evolution by drilling lake basin sediments adjacent to important archeological and paleoanthropological sites. OLO12-1A recovered 139 m of sedimentary and volcaniclastic strata from the Koora lake basin, providing the opportunity to compare paleoenvironmental influences over the past million years with the parallel record exposed at the Olorgesailie archeological site 24 km to the north. To refine our ability to link the core and outcrop paleoenvironmental records, we have developed a robust, high-resolution chronostratigraphic model of the core, based on a dense series of $^{40}Ar/^{39}Ar$ ages and identification of the Brunhes/Matuyama paleomagnetic boundary. This model incorporates a novel approach to accommodating highly variable sedimentation rates and hiatuses due to landscape exposure and paleosol development in order to linearize the sediment accumulation rate curve. The final age model provides a mechanism for transforming core depths to absolute ages, with realistic uncertainties that will allow accurate temporal correlations between core and outcrop and also to regional and global climate patterns.

The new age model provides a precise foundation for placing the lithostratigraphy of the core in a temporal framework. Sedimentation began soon after emplacement of Magadi Trachyte (1.0837 ± 0.0040 Ma), with low input of volcaniclastic material during a period of lacustrine and subaerial deposition between ~1100 and 500 ka. Differing patterns of siliciclastic and volcaniclastic deposition suggests that the Olorgesailie and Koora Basins were mostly separated during this time, however detrital feldspar ages in dated volcaniclastics suggests commonality in drainage areas, and at least one fluvially deposited Olorgesailie tuff from this interval is also recognized in Koora Basin outcrop exposures.

Predominantly lacustrine facies in both areas between 600 and 500 ka suggest a shared interval of high lake level, whether or not there was a connection via the Koora Graben.

The Koora Basin was likely connected to the Olorgesailie basin by the beginning of the period of northern basin erosion between ~500 and 320 ka. In the Koora Basin, this prominent erosional phase coincided with alternating lacustrine sedimentation and paleosol development plus increasing tephra input. Considerations of rift morphology, drainage patterns, eruptive history of regional volcanic centers, and outcrop tephra accumulations at Olorgesailie suggests that the CKPP was likely the predominant source of the voluminous, coarse, pumiceous tephra in the last ~270 ka record of OLO12-1A. The Koora and Olorgesailie Basins underwent periodic connection/disconnection throughout the post-500 ka interval, ultimately finalized in the inter-connected drainage of today.

Acknowledgments

We gratefully acknowledge support for the Olorgesailie Drilling Project from the National Museums of Kenya, the Oldonyo Nyokie Group Ranch, the Peter Buck Fund for Human Origins Research (Smithsonian), the William H. Donner Foundation (R.P.), the Ruth and Vernon Taylor Foundation (R.P.), Whitney and Betty MacMillan (R.P.), and the Smithsonian's Human Origins Program. Geochronological research was supported by National Science Foundation grant EAR 1322017. R.D. acknowledges support of a Smithsonian Postdoctoral Fellowship and by Geo. X, the Research Network for Geosciences in Berlin and Potsdam, Germany. M. S. acknowledges support from the Swiss National Science Foundation (grant P300P2 158501). Fig. 1 is based on the TanDEM-X Science DEM, granted to S. Riedl by the German Space Agency (© DLR 2017). Research and drilling permits were provided by the Kenyan National Council for Science and Technology, the Kenyan Ministry of Mines, and the National Environmental Management Authority of Kenya, and facilitated by the National Museums of Kenya. We thank DOSECC Exploration Services for drilling supervision, Drilling and Prospecting International (DPI) for drilling services, and the US National Lacustrine Core Facility (University of Minnesota) for core handling, processing and storage facilities. We thank R.B. Owen for his collaboration with the lithologic core description. We are grateful for discussions and ongoing contributions by our colleagues of the HSPDP research groups.

Appendix A. Supplementary data

Supplementary data to this article can be found online at https://doi.org/10.1016/j.quascirev.2019.05.009.

References

Baker, B.H., 1975. Geology and geochemistry of the Ol Doinyo Nyokie trachyte ignimbrite vent complex, south Kenya rift valley. Bull. Volcanol. 39, 4201–4221.
Baker, B.H., Mitchell, J.G., 1976. Volcanic stratigraphy and geochronology of the Kedong–Olorgesailie area and the evolution of the South Kenya rift valley. J. Geol. Soc. 132467–132484.
Baker, B.H., 1986. Tectonics and volcanism of the southern Kenya Rift Valley and its influence on rift sedimentation. In: Tiercelin, J.J. (Ed.), Sedimentation in the African Rifts. Blackwell Scientific Publications, Oxford, pp. 45–57.
Behrensmeyer, A.K., Hook, R.W., 1992. Paleoenvironmental contexts and taphonomic modes in the terrestrial fossil record. In: Behrensmeyer, A.K., Damuth, J.D., DiMichele, W.A., Potts, R., Sues, H.-D., Wing, S.L. (Eds.), Terrestrial Ecosystems through Time. University of Chicago Press, Chicago, pp. 15–136.
Behrensmeyer, A.K., Potts, R., Deino, A., Ditchfield, P., 2002. Olorgesailie, Kenya: a million years in the life of a rift basin. In: Renaut, R.W., Ashley, G.M. (Eds.), Sedimentation in Continental Rifts.
Behrensmeyer, A.K., Potts, R., Deino, A., 2018. The Oltulelei Formation of the southern Kenyan Rift Valley: a chronicle of rapid landscape transformation over the last 500 k.y. Geol. Soc. Am. Bull. 130 (9–10), 1474–1492.
Bergner, A.G.N., Strecker, M.R., Trauth, M.H., Deino, A., Gasse, F., Blisniuk, P., Duehnforth, M., 2009. Tectonic and climatic control on evolution of rift lakes in the Central Kenya Rift, East Africa. Quat. Sci. Rev. 28 (25–26), 2804–2816.
Blaauw, M., Christen, J.A., 2011. Flexible paleoclimate age-depth models using an autoregressive gamma process. Bayesian Anal. 6457–6474.
Blegen, N., Brown, F.H., Jicha, B.R., Binetti, K.M., Faith, J.T., Ferraro, J.V., Gathogo, P.N., Richardson, J.L., Tryon, C.A., 2016. The Menengai Tuff: a 36 ka widespread tephra and its chronological relevance to Late Pleistocene human evolution in East Africa. Quat. Sci. Rev. 152152–152168.
Brooks, A.S., Yellen, J.E., Potts, R., Behrensmeyer, A.K., Deino, A.L., Leslie, D.E., Ambrose, S.H., Ferguson, J.R., d'Errico, F., Zipkin, A.M., Whittaker, S., Post, J., Veatch, E.G., Foecke, K., Clark, J.B., 2018. Long-distance stone transport and pigment use in the earliest Middle Stone Age. Science 360 (6384), 90–94.
Campisano, C.J., Cohen, A.S., Arrowsmith, J.R., Asrat, A., Behrensmeyer, A.K., Brown, E.T., Deino, A.L., Deocampo, D.M., Feibel, C.S., Kingston, J.D., Lamb, H.F., Lowenstein, T.K., Noren, A., Olago, D.O., Owen, R.B., Pelletier, J.D., Potts, R., Reed, K.E., Renaut, R.W., Russell, J.M., Russell, J.R., Schäbitz, F., Stone, J.R., Trauth, M.H., Wynn, J.G., 2017. The hominin sites and paleolakes drilling project: acquiring high-resolution paleoclimate records from the east African Rift system and their implications for understanding the environmental context of hominin evolution. PaleoAnthropology 1–43.
Cleveland, D.M., Atchley, S.C., Nordt, L.C., 2007. Continental sequence stratigraphy of the Upper Triassic (Norian-Rhaetian) Chinle strata, northern New Mexico, USA: allocyclic and autocyclic origins of paleosol-bearing alluvial successions. J. Sediment. Res. 77 (11–12), 909–924.
Cohen, A., Campisano, C., Arrowsmith, R., Asrat, A., Behrensmeyer, A.K., Deino, A., Feibel, C., Hill, A., Johnson, R., Kingston, J., Lamb, H., Lowenstein, T., Noren, A., Olago, D., Owen, R.B., Potts, R., Reed, K., Renaut, R., Schaebitz, F., Tiercelin, J.J., Trauth, M.H., Wynn, J., Ivory, S., Brady, K., O'Grady, R., Rodysill, J., Githiri, J., Russell, J., Foerster, V., Dommain, R., Rucina, S., Deocampo, D., Russell, J., Billingsley, A., Beck, C., Dorenbeck, G., Dullo, L., Feary, D., Garello, D., Gromig, R., Johnson, T., Junginger, A., Karanja, M., Kimburi, E., Mbuthia, A., McCartney, T., McNulty, E., Muiruri, V., Nambiro, E., Negash, E.W., Njagi, D., Wilson, J.N., Rabideaux, N., Raub, T., Sier, M.J., Smith, P., Urban, J., Warren, M., Yadeta, M., Yost, C., Zinaye, B., 2016. The Hominin Sites and Paleolakes Drilling Project: inferring the environmental context of human evolution from eastern African rift lake deposits. Sci. Drill. 211–216.
CSDCO, 2011. Tool for Microscopic Identification.
Deino, A., Potts, R., 1990. Single-crystal Ar-40/Ar-39 dating of the Olorgesailie Formation, southern Kenya rift. J. Geophys. Res. 95 (B6), 8453–8470.
Deino, A.L., Kingston, J.D., Glen, J.M., Edgar, R.K., Hill, A., 2006. Precessional forcing of lacustrine sedimentation in the late Cenozoic Chemeron Basin, Central Kenya Rift, and calibration of the Gauss/Matuyama boundary. Earth Planet. Sci. Lett. 247 (1–2), 41–60.
Deino, A.L., Scott, G.R., Saylor, B., Alene, M., Angelini, J.D., Haile-Selassie, Y., 2010. Ar-40/Ar-39 dating, paleomagnetism, and tephrochemistry of Pliocene strata of the hominid-bearing Woranso-Mille area, west-central Afar Rift, Ethiopia. J. Hum. Evol. 58 (2), 111–126.
Deino, A.L., Behrensmeyer, A.K., Brooks, A.S., Yellen, J.E., Sharp, W.D., Potts, R., 2018. Chronology of the acheulean to middle stone age transition in eastern Africa. Science 360 (6384), 95–98.
deMenocal, P.B., 1995. Plio-pleistocene african climate. Science 270 (5233), 53–59.
Ebinger, C., Scholz, C.A., Busby, C., Azor, A., 2012. Continental Rift Basins: the East African Perspective, pp. 185–208.
Fleck, R.J., Sutter, J.F., Elliot, D.H., 1977. Interpretation of discordant 40Ar/39Ar age-spectra of Mesozoic tholeiites from Antarctica. Geochem. Cosmochim. Acta 4115–4132.
Foerster, V., Junginger, A., Langkamp, O., Gebru, T., Asrat, A., Umer, M., Lamb, H.F., Wennrich, V., Rethemeyer, J., Nowaczyk, N., Trauth, M.H., Schaebitz, F., 2012. Climatic change recorded in the sediments of the Chew Bahir basin, southern Ethiopia, during the last 45,000 years. Quat. Int. 274, 25–37 (Temporal and spatial corridors of Homo sapiens sapiens population dynamics during the Late Pleistocene and Early Holocene).
Foster, A., Ebinger, C., Mbede, E., Rex, D., 1997. Tectonic development of the northern Tanzanian sector of the east African rift system. J. Geol. Soc. 154689–154700.
Garcin, Y., Junginger, A., Melnick, D., Olago, D.O., Strecker, M.R., Trauth, M.H., 2009. Late Pleistocene-Holocene rise and collapse of lake Suguta, northern Kenya rift. Quat. Sci. Rev. 28 (9–10), 911–925.
Garcin, Y., Schildgen, T.F., Acosta, V.T., Melnick, D., Guillemoteau, J., Willenbring, J., Strecker, M.R., 2017. Short-lived increase in erosion during the african humid period: evidence from the northern Kenya rift. Earth Planet. Sci. Lett. 45958–45969.
Gawthorpe, R.L., Leeder, M.R., 2000. Tectono-sedimentary evolution of active extensional basins. Basin Res. 12195–12218.
Gibbons, A., 2013. How a Fickle climate made us human. Science 341 (6145), 474–479.
Grimm, E.C., 2011. High-resolution age model based on AMS radiocarbon ages for Kettle Lake, North Dakota, USA. Radiocarbon 5339–5353.
Guth, A., Wood, J., 2013. Geology of the Magadi Area. Kenya.
Haslett, J., Parnell, A.C., 2008. A simple monotone process with application to radiocarbon-dated depth chronologies. J. R. Stat. Soc. Ser. C (Appl. Stat.) 57399–57418.
Hastings, W.K., 1970. Monte Carlo sampling methods using Markov chains and their applications. Biometrika 97–109.
Hendrie, D.B., Kusznir, N.J., Morley, C.K., Ebinger, C.J., 1994. Cenozoic extension in northern Kenya - a quantitative model of rift basin development in the Turkana

region. Tectonophysics 236 (1–4), 409–438.
Isaac, G.L., 1977. Olorgesailie: Archaeological Studies of a Middle Pleistocene Lake Basin in Kenya. Chicago University Press, Chicago.
Jenny, H., 1941. Factors of Soil Formation: A System of Quantitative Pedology. McGraw-Hill, New York.
Johnson, T.C., Werne, J.P., Brown, E.T., Abbott, A., Berke, M., Steinman, B.A., Halbur, J., Contreras, S., Grosshuesch, S., Deino, A., Lyons, R.P., Scholz, C.A., Schouten, S., Damste, J.S.S., 2016. A progressively wetter climate in southern East Africa over the past 1.3 million years. Nature 537 (7619), 220.
Keller, C.B., 2018. Chron.jl: A Bayesian Framework for Integrated Eruption Age and Age-Depth Modelling.
Kelts, K.R., 2003. Components in lake sediments: smear slide identification. In: Valeo-Garcés, B.L. (Ed.), Limnogeology in Spain: a Tribute to Kerry R. Kelts. Consejo Superior de Investigaciones Científicas, Madrid, pp. 59–72.
Kirschvink, J.L., 1980. The least-squares line and plane and the analysis of palaeomagnetic data, 62 (3), 699–718.
Lee, J.-Y., Marti, K., Severinghaus, J.P., Kawamura, K., Yoo, H.-S., Lee, J.B., Kim, J.S., 2006. A redetermination of the isotopic abundances of atmospheric Ar. Geochem. Cosmochim. Acta 704507–704512.
Lupien, R.L., Russell, J.M., Feibel, C., Beck, C., Castaneda, I., Deino, A., Cohen, A.S., 2018. A leaf wax biomarker record of early Pleistocene hydroclimate from West Turkana, Kenya. Quat. Sci. Rev. 186225–186235.
Macdonald, R., Scaillet, B., 2006. The central Kenya peralkaline province: insights into the evolution of peralkaline salic magmas. Lithos 9159–9173.
Mana, S., Furman, T., Turrin, B.D., Feigenson, M.D., Swisher III, C.C., 2015. Magmatic activity across the east african north Tanzanian divergence zone. J. Geol. Soc. 172 (3), 368–389.
McDougall, I., Harrison, T.M., 1999. Geochronology and Thermochronology by the 40Ar/39Ar Method. Oxford University Press, Oxford, New York.
Melnick, D., Garcin, Y., Quinteros, J., Strecker, M.R., Olago, D., Tiercelin, J.-J., 2012. Steady rifting in northern Kenya inferred from deformed Holocene lake shorelines of the Suguta and Turkana basins. Earth Planet. Sci. Lett. 331335–331346.
Min, K.W., Mundil, R., Renne, P.R., Ludwig, K.R., 2000. A test for systematic errors in Ar-40/Ar-39 geochronology through comparison with U/Pb analysis of a 1.1-Ga rhyolite. Geochim. Cosmochim. Acta 64 (1), 73–98.
Mollel, G.F., Swisher III, C.C., 2012. The Ngorongoro volcanic highland and its relationships to volcanic deposits at Olduvai Gorge and east African Rift volcanism. J. Hum. Evol. 63 (2), 274–283.
Niespolo, E.M., Rutte, D., Deino, A.L., Renne, P.R., 2017. Intercalibration and age of the Alder Creek sanidine Ar-40/Ar-39 standard. Quat. Geochronol. 39205–39213.
Noren, A.J., Bierman, P.R., Steig, E.J., Lini, A., Southon, J., 2002. Millennial-scale storminess variability in the northeastern United States during the Holocene epoch. Nature 419821–419824.
Ogg, J.G., Gradstein, F.M., Ogg, J.G., Schmitz, M.D., Ogg, G.M., 2012. Geomagnetic Polarity Time Scale, pp. 85–113.
Olaka, L.A., Odada, E.O., Trauth, M.H., Olago, D.O., 2010. The sensitivity of East African rift lakes to climate fluctuations. J. Paleolimnol. 44 (2), 629–644.
Owen, R.B., Muiruri, V.M., Lowenstein, T.K., Renaut, R.W., Rabideaux, N., Luo, S., Deino, A.L., Sier, M.J., Dupont-Nivet, G., McNulty, E.P., Leet, K., Cohen, A., Campisano, C., Deocampo, D., Shen, C.-C., Billingsley, A., Mbuthia, A., 2018. Progressive Aridification in East Africa over the Last Half Million Years and Implications for Human Evolution. National Academy of Sciences.
Pennisi, E., 2013. Out of the Kenyan mud, an ancient climate record. Science 341 (6154), 476–479.
Potts, R., 1994. Variables versus models of early Pleistocene hominid land-use. J. Hum. Evol. 27 (1–3), 7–24.
Potts, R., 1996. Evolution and climate variability. Science 273 (5277), 922–923.
Potts, R., 2013. Hominin evolution in settings of strong environmental variability. Quat. Sci. Rev. 73, 1–13.
Potts, R., Behrensmeyer, A.K., Faith, J.T., Tryon, C.A., Brooks, A.S., Yellen, J.E., Deino, A.L., Kinyanjui, R., Clark, J.B., Haradon, C.M., Levin, N.E., Meijer, H.J.M., Veatch, E.G., Owen, R.B., Renaut, R.W., 2018. Environmental dynamics during the onset of the middle stone age in eastern Africa. Science 360 (6384), 86.
Ramsey, C.B., 2008. Deposition models for chronological records. Quat. Sci. Rev. 2742–2760.
Robertson, E.A.M., Biggs, J., Cashman, K.V., Floyd, M.A., Vye-Brown, C., 2016. Influence of Regional Tectonics and Pre-existing Structures on the Formation of Elliptical Calderas in the Kenyan Rift. Geological Society of London.
Rothwell, R.G., 1989. Minerals and Mineraloids in Marine Sediments. An Optical Identification Guide. Elsevier, London.
Sagnotti, L., 2013. Demagnetization Analysis in Excel (DAIE). An open source workbook in Excel for viewing and analyzing demagnetization data from paleomagnetic discrete samples and u-channels. Ann. Geophys. 56 (1).
Scholz, C.A., Johnson, T.C., Cohen, A.S., King, J.W., Peck, J.A., Overpeck, J.T., Talbot, M.R., Brown, E.T., Kalindekafe, L., Amoako, P.Y.O., Lyons, R.P., Shanahan, T.M., Castaneda, I.S., Heil, W., Forman, S.L., McHargue, L.R., Beuning, K.R., Gomez, J., Pierson, J., 2007. East African megadroughts between 135 and 75 thousand years ago and bearing on early-modern human origins. Proc. Natl. Acad. Sci. U.S.A. 104 (42), 16416–16421.
Sherrod, D.R., Magigita, M.M., Kwelwa, S., 2013. Geologic Map of Oldonyo Lengai (Oldoinyo Lengai) and Surroundings, Arusha Region, United Republic of Tanzania. U.S. Geological Survey Open-File Report, 2013-130665 p.
Sier, M.J., Langereis, C.G., Dupont-Nivet, G., Feibel, C.S., Joordens, J.C.A., van der Lubbe, J.F., Beck, C.C., Olago, D., Cohen, A., WTK, S.T.M., 2017. The top of the Olduvai Subchron in a high-resolution magnetostratigraphy from the west Turkana core WTK13, hominin sites and paleolakes drilling project (HSPDP). Quat. Geochronol. 42117–42129.
Staff, S.S., 2014. Illustrated Guide to Soil Taxonomy 1.0. USDA NRCS, Lincoln.
Stockhecke, M., Sturm, M., Brunner, I., Schmincke, H., Sumita, M., Kipfer, R., Cukur, D., Kwiecien, O., Anselmetti, F.S., 2014. Sedimentary evolution and environmental history of Lake Van (Turkey) over the past 600 000 years. Sedimentology 61 (6), 1830–1861.
Strecker, M.R., Blisniuk, P.M., Eisbacher, G.H., 1990. Rotation of extension direction in the Central Kenya Rift. Geology 18 (4), 299–302.
Targulian, V.O., Krasilnikov, P.V., 2007. Soil system and pedogenic processes: self-organization, time scales, and environmental significance. Catena 71 (3), 373–381.
Tauxe, L., Badgley, C., 1988. Stratigraphy and remanence acquisition of a palaeomagnetic reversal in alluvial Siwalik rocks of Pakistan. Sedimentology 35 (4), 697–715.
Trauth, M.H., 2014. A new probabilitistic technique to build an age model for complex stratigraphic sequences. Quat. Geochronol. 2265–2271.
Trauth, M.H., Deino, A.L., Bergner, A.G.N., Strecker, M.R., 2003. East African climate change and orbital forcing during the last 175 kyr BP. Earth Planet. Sci. Lett. 206 (3–4), 297–313.
Verschuren, D., Damste, J.S.S., Moernaut, J., Kristen, I., Blaauw, M., Fagot, M., Haug, G.H., Members C.H.A.L.L.A.C.E.A.P., 2009. Half-precessional dynamics of monsoon rainfall near the East African equator. Nature 462 (7273), 637–641.
Vrba, E.S., 1992. Mammals as a key to evolutionary theory. J. Mammal. 73 (1), 1–28.
Wright, T.J., Ebinger, C., Biggs, J., Ayele, A., Gezahegn, Y., Yirgu, D., Keir, D., Stork, A., 2006. Magma-maintained rift segmentation at continental rupture in the 2005 Afar dyking episode. Nature 442291–442294.
Zijderveld, J.D.A., 1967. Demagnetization of rocks: analysis of results. In: Collison, P.A., Creer, K.M., Runcorn, S.K. (Eds.), Methods in Paleomagnetism. Elsevier, Amsterdam.